J Biosci (2024)49:4
DOI: 10.1007/s12038-023-00367-x

Molecular transformations and self-association in anthocyanin pigment patterns

WEI-YU HSU[1], PATRICK D. SHIPMAN[2]* and STEPHEN THOMPSON[3]

[1]*Department of Mathematics, Colorado State University, 1874 Campus Delivery, Fort Collins, CO 80523-1874, USA*

[2]*Present Address: Department of Mathematics and Graduate Interdisciplinary Program in Applied Mathematics, The University of Arizona, 617 N. Santa Rita Ave., Tucson, AZ 85721-0089, USA*

[3]*Department of Chemistry, Colorado State University, 1872 Campus Delivery, Fort Collins, CO 80523-1872, USA*

**Corresponding author (Email, patrickshipman@math.arizona.edu)*

MS received 3 January 2023; accepted 2 May 2023

Spatial patterns of red, purple, and blue colors due to plant pigments called anthocyanins appear in a wide variety of flower petals. Activator and inhibitor proteins involved in anthocyanin synthesis in *Mimulus* (monkeyflowers) have been identified, and an activator–inhibitor system based on the classic Gierer–Meinhardt system has been proposed as a mathematical model. Analysis in this paper provides a prediction for the critical value of a dimensionless parameter, the ratio of the degradation rate constants of the inhibitor and activator, for pattern formation to occur, and numerical simulations demonstrate the potential for this system to form disordered hexagonal or stripe patterns. We provide experimental evidence for spatial variation in total anthocyanin concentration and for concentration-dependent anthocyanin association. Extending the mathematical model to include anthocyanin transport and diffusion, a series of molecular transformations encompassing acid-base and hydration (speciation) reactions, and self association, we predict that spatial color patterns are accompanied by complex spatial variation in the degree of self association. An important consequence of these studies is a proposal that anthocyanin association allows for colored anthocyanin species to be present in large mole fractions in cell vacuoles despite the fact that the typical vacuolar pH range favors the formation of colorless species.

Keywords. Anthocyanins; plant pigments; pattern formation; activator–inhibitor system; association

1. Introduction

The beautiful pink, red, purple, and blue colors observed in flowers, fruits, leaves, and stems of the plant kingdom derive primarily from a class of water-soluble cell pigments called anthocyanins (Lee and Gould 2002). These biologically active chemicals play diverse roles in plant cell biology and ecology (Alappat and Alappat 2020): Anthocyanins participate together with chlorophyll and carotenoids (lipid-soluble pigments responsible for yellow and orange colors) in the optical–chemical pathways of energy transduction in plant cells and act as phytophotoprotectants (Field *et al.* 2001; da Silva *et al.* 2012; Zheng *et al.* 2021). These molecules contribute to pH buffering that is crucial to the regulation of cellular processes (Leydet *et al.* 2012; Pina *et al.* 2015). Plant cell defense mechanisms can involve anthocyanins (Lev-Yadun and Gould 2009).

Ecologically, pollinators recognize both colors and color patterns in flowers; pollutants or changes in climate that impact these colors have been implicated in plant–pollinator mismatches (Gérard *et al.* 2020; United Nations 2021). Spatial patterns of coloration due to varying anthocyanin concentrations are observed on many flowers (Medel *et al.* 2003; Hsu *et al.* 2015; Ding *et al.* 2020; Bhati *et al.* 2021). See figure 1 for some examples.

Published online: 19 December 2023

Figure 1. Anthocyanin patterns on petals: Top row from left to right: patterns on flowers of *Paubrasilia echinata* (Brazilwood), *Chilopsis linearis* (desert willow), *Viola wittrockiana* Gams (yellow pansy), and *Salvia yangii* (Russian sage). Bottom row: patterns on petunia petals.

Spatial patterns in biological systems are often due to feedback loops between activators and inhibitors (Young 1984; Turing 1990). The simplest such pattern-forming system consists of one species of activator molecule and one species of inhibitor molecule. The activator promotes its own production as well as that of the inhibitor, and the inhibitor inhibits the production of the activator. Identifying activator and inhibitor molecules involved in anthocyanin synthesis for flowers of the genus *Mimulus* (monkeyflowers) has been accomplished by Yuan *et al.* (2014) and Ding *et al.* (2020). These authors show a R2R3-MYB protein to be a molecular activator for itself as well as for anthocyanin production and that a R3-MYB protein inhibits activator production.

Ding *et al.* (2020) propose a modification of the classical Gierer–Meinhardt (GM) activator–inhibitor system as a mathematical model for the monkeyflower. Their numerical simulations of this model reproduce a range of spatial activator patterns that are similar to spatial anthocyanin patterns observed on monkeyflower petals. Amazingly, these researchers can also experimentally modify a parameter in their model, namely the degradation rate constant for the inhibitor, and observe changes in the observed anthocyanin pattern that match predictions of their model. Further, they show these modifications impact the attraction of bumblebee pollinators to these flowers.

There are over 700 known anthocyanins (as glycosides), comprising 27 different aglycone chromophore structures, although 6 are most common: pelargonin, cyanidin, delphinidin, peonidin, petunidin, and malvidin. Each of these anthocyanins can undergo an incredible number of structural changes which are pH, metal ion, temperature, light, and concentration dependent (Leydet *et al.* 2012; Fernandes *et al.* 2015; Pina *et al.* 2015). Anthocyanins are typically extracted from plant sources with acidified solvents (e.g. methanonl/HCl or CF_3COOH). Extracts are then studied spectroscopically under different solution conditions. Figure 2 shows the colour changes for red cabbage (*Brassica Rubra captitula*) and red raddish (*Raphanus sativus*) extracts buffered at a range of pH values. Also shown is the effect of pH (pH 1 to 12.5 in 0.5 increments) on a single, pure, anthocyanin, malvin. Malvin-derived anthocyanins are found in grapes, eggplant, blueberries, and the petals of *Primula* and petunia.

Various spectroscopic techniques (such as UV/VIS, NMR, and CD) have shown that, *in vitro*, aqueous solutions of anthocyanins exhibit concentration-dependent self association in both the red and purple/blue forms (González-Manzano *et al.* 2008; Hoshino *et al.* 1981a, b; Hoshino 1991, 1992; Leydet *et al.* 2012; Mendoza *et al.* 2020; Padayachee *et al.* 2012). The red form is a flavylium cation, and the purple/blue form is a quinoidal base; details are provided in section 3.1. Association of anthocyanins with other, colorless, co-pigments can also occur. These associative processes can eventually produce nanoparticles and structures called anthocyanic vacuolar incusions (AVIs) which are not in solution. These *in vitro* studies indicate that association becomes significant at anthocyanin concentrations of 10^{-3} M and greater (Wagner

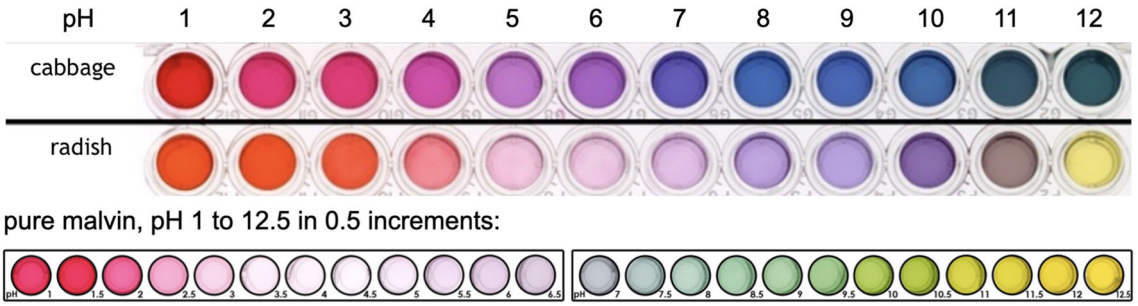

Figure 2. Anthocyanin extracts from cabbage and radish, and pure malvin, at a range of pH values. These extracts were prepared by S Thompson (Thompson 2001, 2010).

1979; Yamada *et al.* 2009). One of us (S Thompson) used microscopy-aided microspectrometry of epidermal peels of flowers and berries to obtain UV/VIS absorbance and fluorescence spectra. The vacuolar environment of epidermal cells is different from that of an aqueous solution, but in the ground and excited states, spectral parameters seem to be similar to those in purely aqueous solutions. These studies reveal that *in vivo* anthocyanin concentrations often exceed 10^{-2} M, sometimes approaching 0.5–1 M in berries. The microscopic images of plant epidermal cells in figure 3 illustrate association of anthocyanins at high concentrations *in vivo*, either by self association or co-pigmentation.

Stripe patterns in *Salvia yangii*, Russian sage, as shown in figure 1 (first row, forth column), may serve as nectar guides for pollinators. A closer examination of these stripe patterns leads to a key motivation for this paper, namely to model the spatial variation in anthocyanin intensity and association. As observed by eye or in the 100× microscopic image of figure 4(a), there appears to be sharp contrast between the purple stripes against their white background. However, magnifications at 200× in figure 4(d), 400× in figure 4(b), and 600× in figure 4(c) reveal a hierarchy of pigmentation: cells at the center of the stripes are deep purple, cells at the stripe borders are generally more pale, and cells further from the stripes are pale purple or white.

Probing the stripes of *S. yangii* by performing pH changes provides evidence that the purple pigment is, in fact, anthocyanin. The purple cells in the stripe shown in figure 4(d) change to red as HCl vapor diffuses across the plant sample from the upper right corner, as shown in figure 4(e). Interestingly, even the formerly white cells show some evidence of red color as the vapor diffuses across. The same region, photographed under fluorescence while excited by a 530 nm green laser and after HCl has diffused across the entire surface, shows strong fluorescence in the regions that were originally white, but darkness prevails along the stripe. We interpret this as evidence that the anthocyanin in the stripe has converted to the red form, which does not fluoresce. See section 4.2 for further interpretation of these results in terms of total anthocyanin concentration, as graphed in figure 15.

The blue cells of *Clitoria ternatea* (butterfly pea), shown in figure 4(g), similarly undergo a transition from blue to red color as HCl vapor diffuses across from the right in figure 4(h). *Allium cepa* (red onion cells) undergo the opposite transformation from red as NH_3 vapor diffuses across a sample from the upper left corner in figure 4(i). The images in figure 4(j–l) show

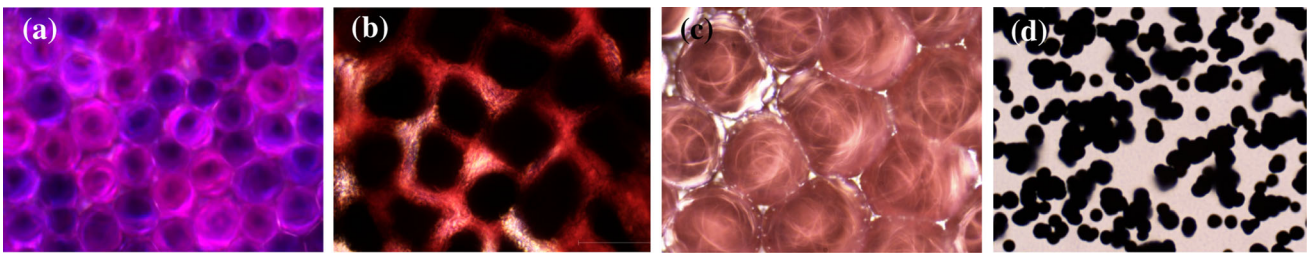

Figure 3. Microscope images of pigmented plant cells and anthocyanin complexes. Various phases of anthocyanin complexes are present in cells of (**a**) purple petunia and (**b**) blueberry. (**c**) Anthocyanins associated with microtubules in geranium cells. (**d**) These black particles remained after an acidic solution of the anthocyanin cyanidin 3-glucoside evaporated. Samples were prepared and imaged by S Thompson.

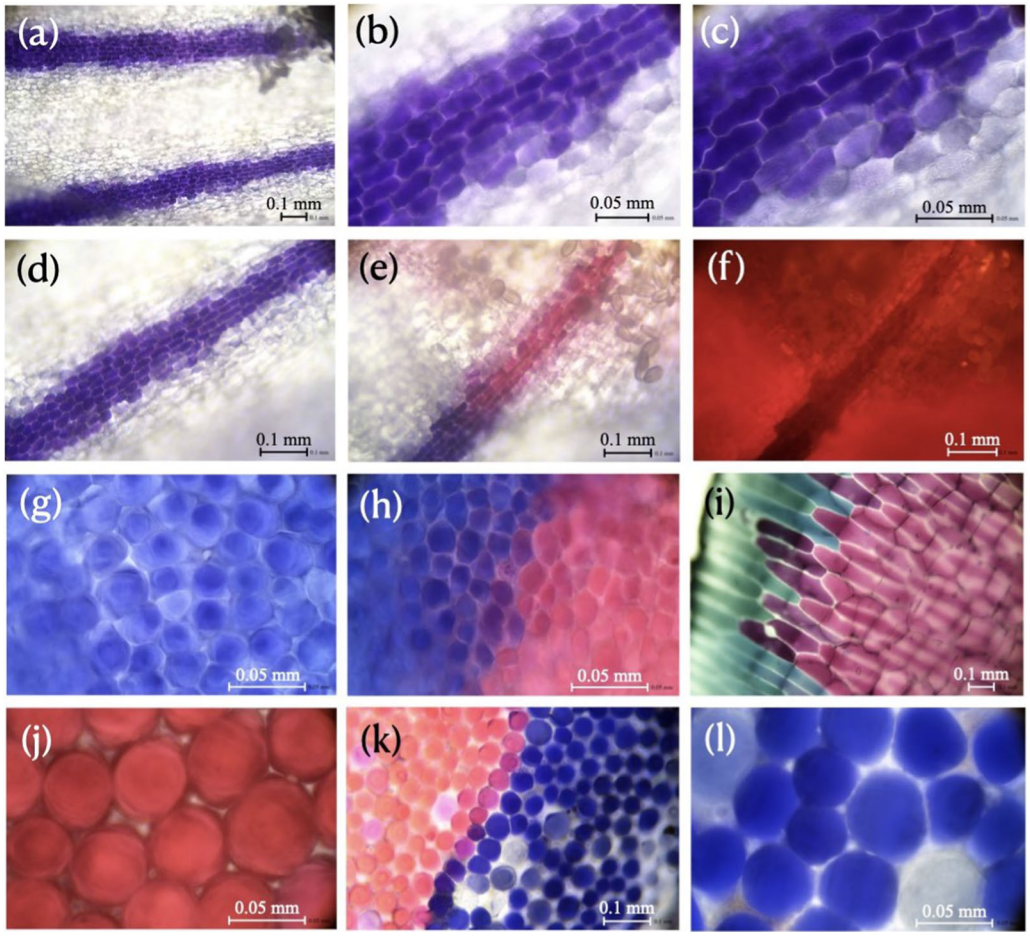

Figure 4. Microscopic images of anthocyanin patterns in flower petals. Panels (**a**–**f**) show cells of *Salvia yangii* (Russian sage) at magnifications (**a**) 100×, (**b**) 400×, (**c**) 600×, and (**d**–**f**) 200×. Panels (**d**–**f**) show the same region of an *S. yangii* stripe. HCl vapor was allowed to diffuse across the sampled region of the petal. The original coloration pattern is shown in panel (**d**); the purple cells turn red as HCl vapor diffuses across the region from the upper right corner of the panel, as shown in panel (**e**). Panel (**f**) shows a fluorescence image of the region excited with a 530 nm green laser. Panels (**g**–**h**) show a similar transformation of color in cells of *Clitoria ternatea* (butterfly pea). Panel (**g**) shows the original sample which changes from blue to red as HCl vapor diffuses in from the right, as shown in panel (**h**). Cells lose their red color as NH_3 vapor diffuses from the upper left across a sample of *Allium cepa* (red onion) in panel (**i**). *Pelargonium* (orange geranium) cells originally exhibit a red color as shown in panel (**j**) but turn blue as NH_3 vapor diffuses across the sample from the right as shown in panel (**k**) and in the image of the cells under higher magnification in panel (**l**).

a transformation of red geranium cells as the NH_3 vapor diffuses across a sample from the right.

The model proposed by Ding *et al.* involves only the activator and the inhibitor; they assume that the anthocyanin is present at spatial locations where the activator exceeds a threshold value. Anthocyanins are synthesized as colorless precursors in the cytoplasm of the epidermal cells. They are then transported across the tonoplast membrane into the vacuole (Poustka *et al.* 2007; Sun *et al.* 2012; Chanoca *et al.* 2015), a cellular compartment which comprises 90% of the cell volume. The pH in the cytoplasm is approximately 7, whereas the pH in the vacuole ranges from 3 to 6. The pH of the vacuole allows for anthocyanins to undergo the structural changes to colored forms as illustrated in figure 2 and subsequently also self association or association with other molecules.

In this paper, we first provide a linear stability analysis of the modified Gierer–Meinhardt (mGM) model proposed by Ding *et al.* (2020). This allows us to determine the critical value of a dimensionless bifurcation parameter, the ratio of the degradation rate constants of the inhibitor and activator, for pattern formation to occur by a Turing instability. We find, through numerical simulations, disordered hexagonal lattice patterns of two types: 'up' ('down') hexagon patterns for which the centers of the hexagons correspond to maxima (minima) of the activator

concentration. Next, we propose an extension of the mGM model to include the activator-induced production of anthocyanin, molecular transformations (anthocyanin speciation), as well as anthocyanin self association. We assume the production rate to be given by a sigmoidal function of the activator (Veitia 2003) and for there to be very low or no diffusion or transport of anthocyanin between cells. A biologically important observation from numerical simulations of this model is that the degree of association can vary dramatically across the pattern, being very strongly associated where there is a high concentration of anthocyanins, but dominated by the monomer where there is a low anthocyanin concentration.

This article is organized as follows: In section 2, we provide a linear stability analysis of the Gierer–Meinhardt model as modified by Ding *et al.* (2020). Numerical simulations of this system close to the bifurcation threshold produce patterns of disordered hexagons and squares. The pattern shifts to disordered stripe patterns or inverted hexagonal patterns far from the bifurcation threshold. In section 3, we describe molecular transformations, which we refer to as *anthocyanin speciation*, provide a mathematical model for speciation, and analyze the pH-dependent steady-state solutions for the model. In section 4, we provide kinetic equations and the associated system of differential equations for anthocyanin self association. The crucial message of this section is that the degree of self association depends nonlinearly on the total anthocyanin concentration. The modified Gierer–Meinhardt model, speciation, self association, and anthocyanin transport from the cytoplasm to the vacuole are all discussed in section 5. Based on this model, we show how spatial patterns involving a variation in the degree of self association occur. The experimental methods for results described throughout the paper are described in section 6. In section 7, we conclude with a discussion of the results and their context in plant pigmentation and physiology.

2. Activator–inhibitor model for anthocyanin synthesis and pattern formation

2.1 *Modified Gierer–Meinhardt model*

The Gierer–Meinhardt model, proposed by its namesakes in 1972 (Gierer and Meinhardt 1972), is a well-known activator–inhibitor model. It is a system of two reaction–diffusion equations that has been applied to model a wide range of problems of pattern formation in morphogenesis. The quantities of interest in the model are the activator A and the inhibitor I. The activator is *autocatalytic* in that the production rate of activator increases with A. The inhibitor inhibits the production of activator; the production rate of activator decreases with increasing I. The activator has a relatively small diffusion coefficient compared with the inhibitor. One can say that the activator is of 'short range', whereas the inhibitor is of 'long range' (Gierer and Meinhardt 1972; Meinhardt 2012; Meinhardt and Gierer 2000). The Gierer–Meinhardt model reads

$$\frac{\partial A}{\partial t} = D_A \triangle A + G_A\left(\frac{A^2}{I} + \widetilde{A_0}\right) - U_A A,$$
$$\frac{\partial I}{\partial t} = D_I \triangle I + G_I A^2 + I_0 - U_I I.$$

The operator Δ is the two-dimensional Laplacian $\Delta = \frac{\partial^2}{\partial x^2} + \frac{\partial^2}{\partial y^2}$ for the two spatial variables x and y. The parameters D_A and D_I are the diffusion coefficients of A and I, respectively. The assumption that the activator is of short range compared with the inhibitor implies that $D_A << D_I$. The molecules degrade with rate constants U_A and U_I and have background production rates $G_A\widetilde{A_0}$ and $I_0 = 0$, respectively. The term $G_A A^2/I$ models the self-activation of A and inhibition of A by I. The activator activates both itself (with a potency G_A) and the inhibitor (with a potency G_I).

The activator–inhibitor model introduced by Ding *et al.* (2020) is a modification of the Gierer–Meinhardt model and consists of a system of partial differential equations for the concentrations A of an activator molecule and I of an inhibitor molecule. The system, which we will refer to as the modified Gierer–Meinhardt (mGM) model, reads

$$\frac{\partial A}{\partial t} = D_A \triangle A + G_A \frac{A^2 + A_0}{I + K} - U_A A \tag{1}$$

$$\frac{\partial I}{\partial t} = D_I \triangle I + G_I A^2 + I_0 - U_I I \tag{2}$$

where the parameters have the same interpretation as for the GM model. The addition of the parameter K to the denominator of the activator production term is the key modification made by Ding *et al.* (2020). This modification prevents the denominator from becoming equal to zero even if the concentration of inhibitor equals zero, and allows them to choose the initial inhibitor concentration to be zero.

Figure 5 shows simulations of the system given by equations (1) and (2) using parameter values suggested

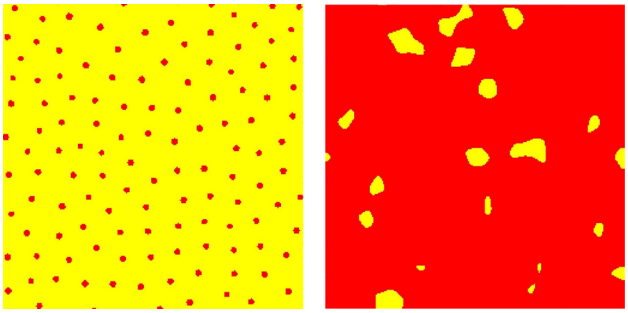

Figure 5. Spatial concentration patterns of activator (left panel) and inhibitor (right panel) at time $t = 10^3$ s, resulting from simulations of the mGM system given by equations (1) and (2). Red (yellow) represents position where the activator or inhibitor concentration is greater (less) than 3. The *prototypical parameter set* as described in the text ($D_A = 0.01, D_I = 0.5, A_0 = 0.01,\ I_0 = 0,\ K = 0.001, G_A = 0.08, G_I = 0.12,\ U_A = 0.03$) was used, together with the choice $U_I = 0.03$. The initial concentration of the activator was $A(0) = 1$ M, and that of the inhibitor was $I(0) = 0$ M. The spatial domain was $0 \leq x, y \leq 50$.

by Ding *et al.* (2020) for their simulations. These authors choose these parameter values without giving units, but they refer to values used for previous studies of the Gierer–Meinhardt model in references (Koch and Meinhardt 1994; Kondo and Asai 1995; Miura and Maini 2004; Kondo and Miura 2010). Following these authors, we focused on how varying the parameter U_I changes the pattern, and therefore simulations in this study will uniformly use what we will call the *prototypical parameter set* $D_A = 0.01, D_I = 0.5, A_0 = 0.01, I_0 = 0, K = 0.001, G_A = 0.08, G_I = 0.12,\ U_A = 0.03$, together with varying choices of U_I ($U_I = 0.03$ for the simulations of figure 5). For all numerical simulations in this study, we employed a Fourier spectral method with periodic boundary conditions and a fourth-order exponential time differencing Runge–Kutta method for the time stepping as the numerical technique (Craster and Sassi 2006) with periodic boundary conditions. Unless otherwise noted, the spatial grid is 256 × 256, and the time step is 0.01.

As Ding *et al.* (2020) suggest, 'subtle changes in simple activator–inhibitor systems are likely essential contributors to the evolution of the remarkable diversity of pigmentation patterns in flowers', and therefore to the diversity of flower–pollinator interactions. Here, we compare the influences of the different parameters. Figure 6 shows further examples of patterns resulting from simulations with parameter values equal to those as for figure 5, except for the degradation rate constant U_I for the inhibitor. Increasing U_I increases the degradation of the inhibitor. There will then be less inhibitor to repress the activator, thereby increasing the concentration of the activator. The degradation constant U_I is the parameter that Ding *et al.* modified experimentally to produce a variety of patterns.

Note that in the simulations of figures 5 and 6, the pattern is a rather disordered arrangement of dots. See figures 4 of 6 in Ding *et al.* (2020) for a comparison of these patterns to dot patterns observed on *Mimulus* flower petals. Patterns of stripes or large blotches, such as those observed in panels of figure 1, are not observed in these simulations, nor are patterns consisting of well-ordered hexagonal lattices as are common in many pattern-forming systems. As discussed in section 7, additional factors, such as petal growth and venation patterns, may come into play to help produce the wide array of patterns observed on petals.

2.2 *Analysis of the modified Gierer–Meinhardt model*

In this section, we first non-dimensionalize the mGM equations. We then perform a linear stability analysis of a homogeneous steady-state solution to these nondimensionalized equations. Ding *et al.* (2020) vary the parameter U_I of the system given by equations (1) and (2) to produce a variety of patterns. Therefore, we are particularly interested in this parameter, and focus on $Q = \frac{U_I}{U_A}$ as a bifurcation parameter. As Q decreases below a critical value Q_T, the homogeneous steady-state solution becomes unstable to periodic disturbances in a Turing instability.

2.2.1 *Nondimensionalization:* The mGM model given by equations (1) and (2) involves three independent variables (two for space and one for time), two dependent variables A and I, and nine parameters. Rescaling the variables and redefining parameters, we can write the system in terms of nondimensional variables and only four nondimensional parameters. First, we note the dimensions of the variables and parameters in the mGM model: denoting the dimensions of a variable or parameter ξ by $[\xi]$, and writing C for 'concentration,' τ for 'time,' and L for 'length,' the dimensions of the original variables and parameters are as follows:

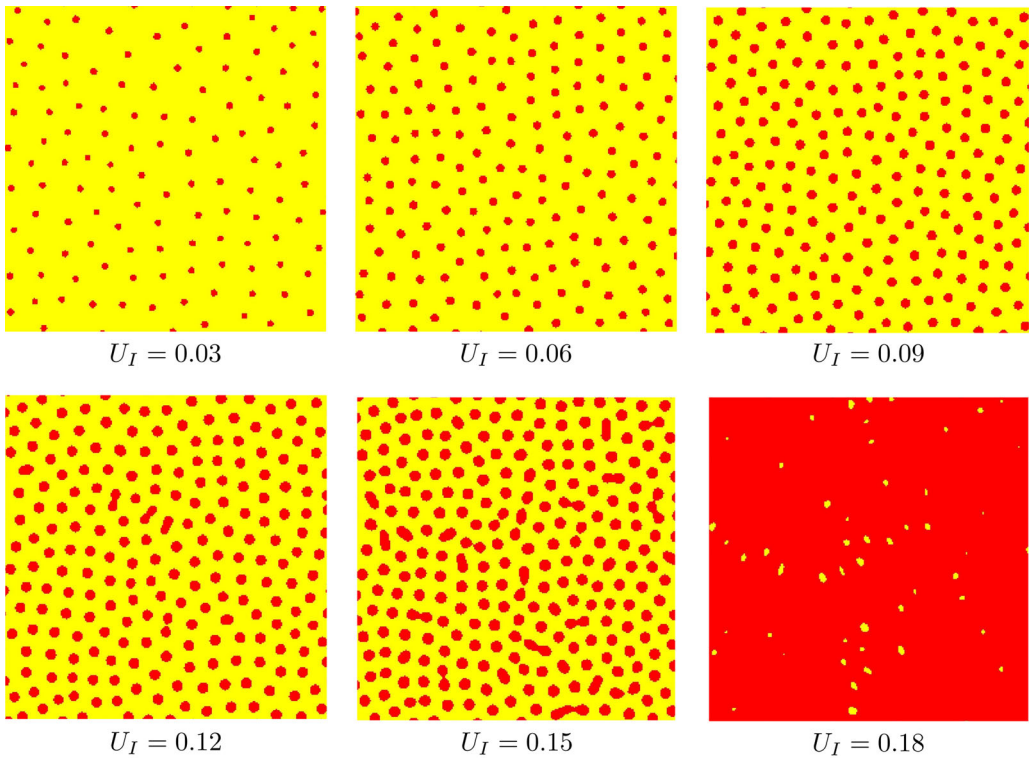

Figure 6. Spatial concentration patterns of activator at time $t = 10^3$ s, resulting from simulations of the mGM system given by equations (1) and (2). Red (yellow) represents position where the activator concentration is greater (less) than 3. The *prototypical parameter set* as described in the text ($D_A = 0.01, D_I = 0.5, A_0 = 0.01, I_0 = 0, K = 0.001, G_A = 0.08, G_I = 0.12,\ U_A = 0.03$) was used, together with the choices of U_I noted below each panel. The initial concentration of the activator was $A(0) = 1$ M, and that of the inhibitor was $I(0) = 0$ M. The spatial domain was $0 \le x, y \le 50$.

$$
\begin{aligned}
[x] =&[y] = L;\ [t] = \tau;\ [A] = [I] = C\\
[D_A] =&[D_I] = L^2\tau^{-1}\\
[G_A] =&\tau^{-1};\ [G_I] = C^{-1}\tau^{-1}\\
[I_0] =&C\tau^{-1};\ [A_0] = C^2;\ [K] = C\\
[U_A] =&[U_I] = \tau^{-1}.
\end{aligned}
$$

Defining dimensionless variables

$$
\begin{aligned}
&u = A_0^{-\frac{1}{2}}A,\ v = K^{-1}I, \tau = U_A t\\
&X = \sqrt{\frac{U_A}{D_I}}x,\ Y = \sqrt{\frac{U_A}{D_I}}y
\end{aligned}
\tag{3}
$$

and parameters

$$
\begin{aligned}
&D = \frac{D_A}{D_I},\ \alpha = \frac{G_A A_0^{1/2}}{U_A K}\ P = \frac{G_I A_0}{U_A K}\\
&Q = \frac{U_I}{U_A},\ R = \frac{I_0}{U_A K}
\end{aligned}
\tag{4}
$$

the mGM models reads

$$
\begin{aligned}
\frac{\partial u}{\partial \tau} &= D\Delta u + \alpha\frac{u^2+1}{v+1} - u \doteq D\Delta u + f_1(u,v)\\
\frac{\partial v}{\partial \tau} &= \Delta v + Pu^2 - Qv + R \doteq \Delta v + f_2(u,v)
\end{aligned}
\tag{5}
$$

where now $\Delta = \frac{\partial^2}{\partial X^2} + \frac{\partial^2}{\partial Y^2}$. We refer to the system (equation 5) as the *dimensionless modified Gierer–Meinhardt model* (dmGM). In terms of the dimensionless parameters, the prototypical parameter values adopted from the work of Ding *et al.* (2020) are $P = 40, \alpha = 800/3, R = 0$, and $D = 0.02$. We refer to these values as the *dimensionless prototypical parameter values*.

2.2.2 *Steady-state solutions and linear stability analysis:* Our analysis of the system (equation 5) begins by finding the simplest type of solution: a homogeneous steady-state solution $u \equiv u^*, v \equiv v^*$, where u^* and v^* are constants. The values u^* and v^* satisfy the system

$$\begin{cases} \alpha\dfrac{(u^*)^2+1}{v^*+1}-u^*=0 \\ P(u^*)^2-Qv^*+R=0 \end{cases} \Rightarrow \begin{cases} v^*=\dfrac{\alpha(u^*)^2-u^*+\alpha}{u^*} \\ v^*=\dfrac{P(u^*)^2+R}{Q} \end{cases} \tag{6}$$

Then u^* is a real-valued solution of the cubic equation $P(u^*)^3-\alpha Q(u^*)^2+(R+Q)u^*-\alpha Q=0$. For the parameter values $P=40, Q=1, R=0, \alpha=800/3$, $K=0.001$, there is one real-valued solution, $(u^*,v^*)\simeq(7.3984, 2189.5)$.

The linearization of the system (equation 5) at its equilibrium is

$$\begin{pmatrix} \dfrac{\partial u}{\partial\tau} \\ \dfrac{\partial v}{\partial\tau} \end{pmatrix} = \mathbf{L}\begin{pmatrix} u \\ v \end{pmatrix} \tag{7}$$

where

$$\begin{aligned} \mathbf{L} &= \begin{pmatrix} \dfrac{\partial f_1}{\partial u} & \dfrac{\partial f_1}{\partial v} \\ \dfrac{\partial f_2}{\partial u} & \dfrac{\partial f_2}{\partial v} \end{pmatrix}_{(u^*,v^*)} \\ &= \begin{pmatrix} \alpha\dfrac{2u^*}{v^*+1}-1 & -\alpha\dfrac{(u^*)^2+1}{(v^*+1)^2} \\ 2Pu^* & -Q \end{pmatrix} \\ &= \begin{pmatrix} \dfrac{(u^*)^2-1}{(u^*)^2+1} & -\dfrac{(u^*)^2}{\alpha((u^*)^2+1)} \\ 2Pu^* & -Q \end{pmatrix} \end{aligned} \tag{8}$$

since $v^*+1=\alpha\frac{(u^*)^2+1}{u^*}$.

The characteristic polynomial of the matrix $\mathbf{L}$ is

$$p(\lambda)=\lambda^2-T_0\lambda+J_0 \tag{9}$$

where

$$T_0=\mathrm{Tr}(\mathbf{L})=\frac{(u^*)^2-1}{(u^*)^2+1}-Q \tag{10}$$

and

$$J_0=\det(\mathbf{L})=-Q\frac{(u^*)^2-1}{(u^*)^2+1}+2P\frac{(u^*)^3}{\alpha((u^*)^2+1)} \tag{11}$$

To analyze the stability of the uniform state under nonuniform perturbations, we seek solutions of the form

$$\begin{pmatrix} u \\ v \end{pmatrix} = \begin{pmatrix} u^* \\ v^* \end{pmatrix} + \epsilon\begin{pmatrix} u_k \\ v_k \end{pmatrix} \exp(i\mathbf{k}\cdot\mathbf{x}+\lambda t)+c.c+o(\epsilon^2) \tag{12}$$

where 'c.c.' is the complex conjugate of $\exp(i\mathbf{k}\cdot\mathbf{x}+\lambda t)$. We find that equation (12) is a solution to the linear system

$$\begin{pmatrix} \dfrac{\partial u}{\partial\tau} \\ \dfrac{\partial v}{\partial\tau} \end{pmatrix} = \mathbf{L}\begin{pmatrix} u \\ v \end{pmatrix} + \begin{pmatrix} D\triangle u \\ \triangle v \end{pmatrix} \tag{13}$$

provided that the following dispersion relation between the linear growth rate λ and the wave number $k=|\mathbf{k}|$ holds:

$$p_k(\lambda)=\lambda^2-T_k\lambda+J_k=0 \tag{14}$$

where

$$T_k=T_0-(D+1)k^2 \tag{15}$$

$$J_k=Dk^4+\left(DQ-\frac{(u^*)^2-1}{(u^*)^2+1}\right)k^2+J_0 \tag{16}$$

The real part of the eigenvalue $\lambda_{k_+}=1/2(T_k+\sqrt{T_k^2-4J_k})$ is positive if either (i) $J_k\geq 0$ and $T_k>0$, or (ii) $J_k<0$.

We look for a Turing bifurcation as the parameter Q varies. The Turing bifurcation occurs when $J_k=0$ for some critical wavenumber $k=k_T$ at a critical parameter value $Q=Q_T$. Rewrite J_k as

$$\begin{aligned} J_k &= Dk^4+\left(DQ-\frac{(u^*)^2-1}{(u^*)^2+1}\right)k^2+J_0 \\ &= D\left(k^4+\frac{DQ-\frac{(u^*)^2-1}{(u^*)^2+1}}{D}k^2+\left(\frac{DQ-\frac{(u^*)^2-1}{(u^*)^2+1}}{2D}\right)^2\right) \\ &\quad +J_0-\frac{\left(DQ-\frac{(u^*)^2-1}{(u^*)^2+1}\right)^2}{4D} \end{aligned} \tag{17}$$

for $J_0=\frac{\left(DQ-\frac{(u^*)^2-1}{(u^*)^2+1}\right)^2}{4D}$. Then, $J_k=0$ provided that

$$k^2 = k_T^2 = -\frac{DQ - \frac{(u^*)^2-1}{(u^*)^2+1}}{2D} = \frac{\sqrt{4DJ_0}}{2D} = \sqrt{\frac{J_0}{D}} \quad (18)$$

The critical value of Q is the solution of the equation

$$4DJ_0 = \left(DQ - \frac{(u^*)^2 - 1}{(u^*)^2 + 1}\right)^2 \quad (19)$$

The system given by equations (18) and (19) can be solved numerically to find approximate values of Q_T and k_T given values for the remaining parameters (figure 7). For the dimensionless prototypical parameter values adopted from the work of Ding *et al.* (2020), these values are $Q_T \approx 8.5468$, and $k_T \approx 4.5571$.

2.3 *Numerical simulations of the modified Gierer–Meinhardt model*

The analysis of the modified Gierer–Meinhardt model provided in section 2.2 allowed for the identification of a nondimensional bifurcation parameter $Q = \frac{U_I}{U_A}$ that is proportional to the degradation rate constant for the inhibitor, and also gives the critical value Q_T of this parameter for a Turing bifurcation to occur. Given fixed values of the other four nondimensional parameters, the homogeneous steady-state solution is unstable to a spatially nonhomogeneous pattern for $Q < Q_T$.

Figure 8 shows results of numerical simulations of the mGM model for the prototypical non-dimensional parameter values given in section 2.2, and $Q < Q_T$. Plotted are the spatial plots of the activator concentration for increasing values of time (columns) and for various values of Q (rows). These results show that the nature of the pattern changes significantly as $|Q - Q_T|$ increases. For $Q = 0.99\ Q_T$ (top row of figure 8), the pattern evolves to a steady state that consists of a disordered array of spots. The pattern for $Q = 0.95\ Q_T$ (second row of figure 8) may be described as a disordered array of spots with weak hexagonal order. The isolated dot pattern first gives way to a pattern of ripples with many defects as Q decreases further below Q_T (third row of figure 8). As Q decreases still further, a disordered 'down' hexagon pattern appears, one for which the isolated dots are regions of *low* activator concentration, surrounded by regions of high activator concentration (fourth row of figure 8) (see, for example, Bradley and Shipman 2012) for a similar comparision of 'up' and 'down' hexagonal patterns. An analogous distinction may occur between cheetah and leopard coat patterns (Murray 2001). A nonlinear analysis of the mGM model and a bifurcation diagram for these various kinds of pattern are provided in Hsu (2022). Similarly, a nonlinear analyisis of a Gierer–Meinhardt model with a saturating term is provided by Song *et al.* (2017).

3. Anthocyanin speciaton

3.1 *Chemistry of anthocyanin molecular transformations (speciation)*

To understand the pH-dependent anthocyanin color variation, we start with the chemical structure of anthocyanins. The basic anthocyanin structure is shown as a flavylium cation in figure 9(a). The three

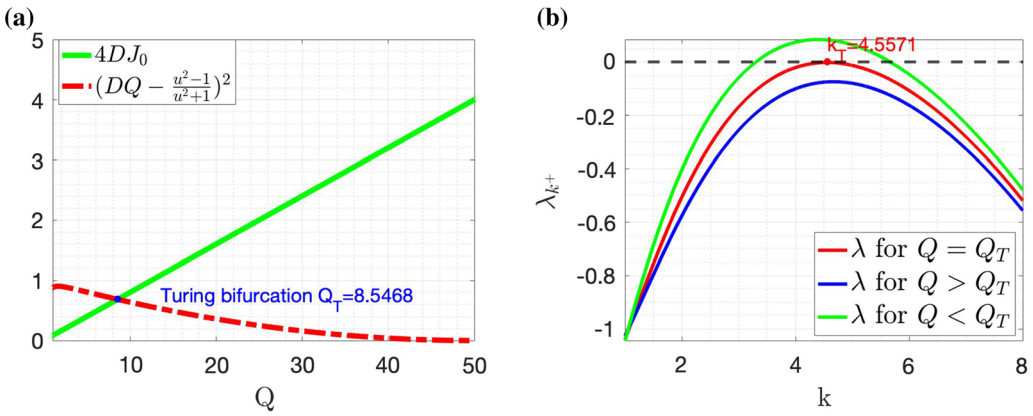

Figure 7. Illustration of the determination of the critical value Q_T of the dimensionless parameter Q for a Turing bifurcation in the mGM model, at a critical wavenumber $k = k_T$ as described in the text. The dimensionless prototypical parameter values ($P = 40, \alpha = 800/3, R = 0$, and $D = 0.02$) were used. Panel (**a**) plots the right- and left-hand sides of equation 19; the intersection point determines Q_T. Panel (**b**) shows the real part of λ_{k_+} for three values of Q, namely $Q = 6.9 > Q_T$ (green curve), $Q = 8.5468 \approx Q_T$ (red curve), and $Q = 10.1 > Q_T$ (blue curve).

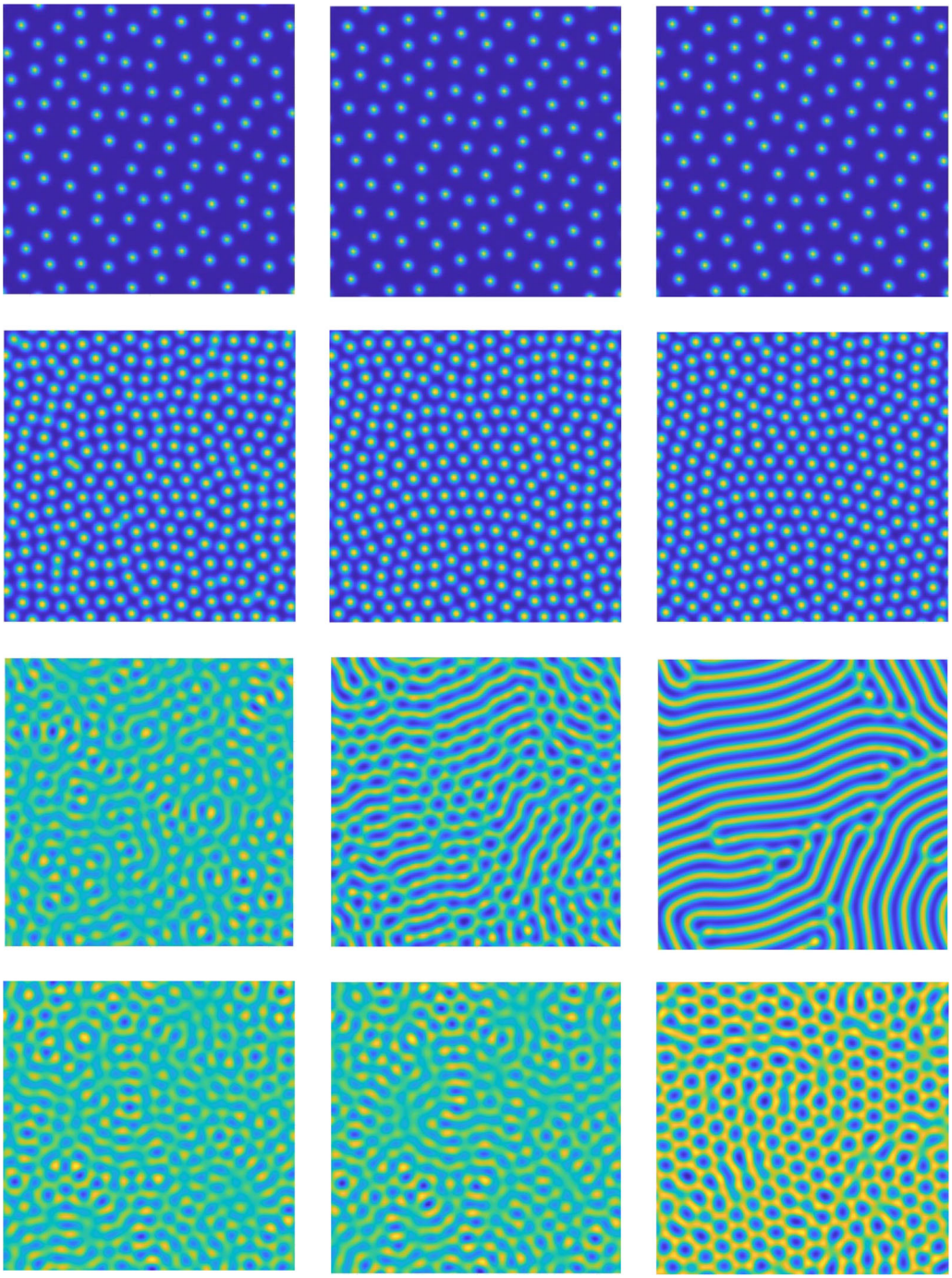

Figure 8. Spatial concentration patterns of activator resulting from simulations of the dmGM system given by the system (5) at various times (columns) and values of the bifurcation parameter Q (rows). Yellow (blue) represents positions where the activator concentration is larger (smaller). The spatial activator pattern is shown at times $t = 180$ s (first column), $t = 720$ s (second column), and $t = 2880$ s (third column). The *dimensionless prototypical parameter set* as described in the text ($P = 40, \alpha = 800/3, Q = 1, R = 0$, and $D = 0.02$) was used. For these values, the critical value for the bifurcation parameter Q is $Q_T = 8.5468$. The parameter Q chosen in the simulations as follows: first row, $Q = 1$; second row, $Q = 6$; third row, $Q = 0.95\ Q_T \simeq 8.1195$; forth row, $Q = 0.99\ Q_T \simeq 8.5468$. The initial concentrations were $u(X, Y, 0) \equiv 1$, and $v(X, Y, 0) \equiv 0$. The spatial domain in the dimensionless spatial variables was $0 \leq X, Y \leq 50\sqrt{\frac{U_A}{D_I}} \approx 12.2474$.

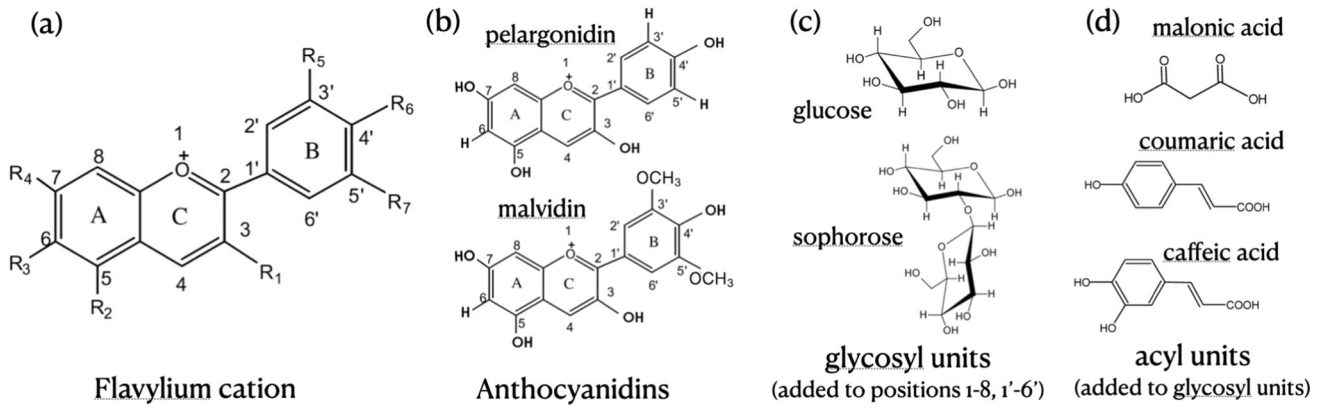

Figure 9. Chemical structure of anthocyanins (**a**) the flavylium cation; (**b**) examples of anthocyanidins produced by substitutions at the positions R_i; (**c**) glycosyl (sugar) units such as glucose and sophorose are added to positions 1–8 and 1′–6′ to produce a water-soluble anthocyanin; (**d**) acyl units may be added to glycosyl units. This figure is adapted from Thompson (2010).

rings of the flavylium cation (labeled as A, B, and C in the figure) form a *chromophore*, the 'box' of quantum-mechanics whose size and number of electrons determine the (absorbance or fluorescence) spectrum. The choices of –H, –OH, or $–OH_3$ groups at the positions R_i determine which of the 27 known types of *anthocyanidin* the molecule is; as examples, the anthocyanidins pelargonidin and malvidin are shown in figure 9(b). Anthocyanidins are insoluble in water, and it is the addition of carbohydrates (glycosyl units) at the positions marked 1–8 and 1′–6′ that turn an anthocyanidin into one of the more than 700 known types of water-soluble anthocyanin. For example, the addition of glucose at positions 3 and 5 produces the anthocyanin malvidin 3, 5-diglucoside, commonly referred to as *malvin* if methoxy groups ($–CH_3$) are added at positions R_5 and R_7. Further modifications may occur, for example, by the addition of acyl units (figure 9(d)) to the sugars. These additions and modifications impact the anthocyanin color, as they donate electrons to the chromophore and change the geometry of the molecule.

Figure 10 depicts a string of fast and slow reactions that occur between what we will call *species* of any given anthocyanin: A^- is a blue anion. Fast acid-base reactions transform A^- into the purple quinoidal base A and turn A into the red flavylium cation AH^+. Slow hydration of AH^+ produces the colorless hemiketal B. Tautomerization produces from B the light yellow *cis*-chalcone C_{cis}, which upon slow isomerization becomes the light yellow-green *trans*-chalcone C_{trans}. The pH of the solution affects the equilibria of these reversible reactions, and thus the species of highest concentration. Important for us is the broad range of colors and the fact that higher pH values favor the reactions moving to the left in the scheme of figure 10 . Of the colored species, the blue anion A^- is the dominant species in alkaline (pH > 7) solutions, the purple A dominates at slightly acidic pH values, and the red cation AH^+ dominates at very acidic pH values. The exact pH range at which each species has the largest concentration depends on the type of anthocyanin.

3.2 *Mathematical model of anthocyanin speciation*

We start with the basic speciation scheme including the species A^- (the blue anion), A (the purple quinoidal base), AH^+ (the red flavylium cation), B (the colorless hemiketal), B^- (the hydroxyl groups on the hemiketal can give off a proton at high pH values), C (the light yellow *cis*-chalcone), and C^- (the light yellow-green *trans*-chalcone), and without association. The chemical reaction scheme is as follows:

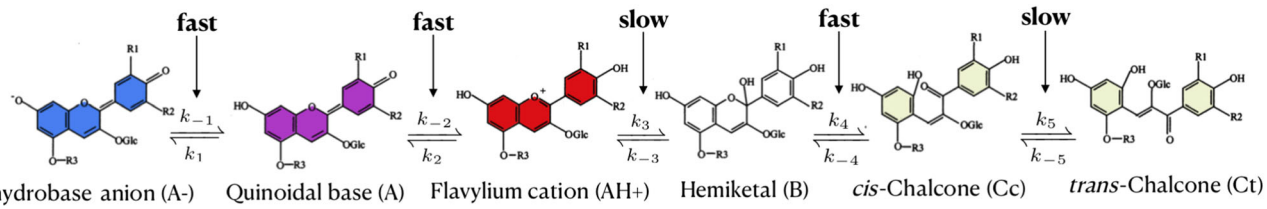

Figure 10. pH-dependent anthocyanin structural changes (adapted from Thompson 2010).

$$
\begin{array}{l}
A^- + H^+ \underset{k_1}{\overset{k_{-1}}{\rightleftharpoons}} A \\
\qquad A + H^+ \underset{k_2}{\overset{k_{-2}}{\rightleftharpoons}} AH^+, \qquad B \underset{k_{-6}}{\overset{k_6}{\rightleftharpoons}} B^- + H^+ \\
\qquad\qquad AH^+ \underset{k_{-3}}{\overset{k_3}{\rightleftharpoons}} B + H^+ \\
\qquad\qquad B \underset{k_{-4}}{\overset{k_4}{\rightleftharpoons}} C \underset{k_{-5}}{\overset{k_5}{\rightleftharpoons}} C^- + H^+
\end{array} \tag{20}
$$

The law of mass action transforms the kinetic equations into the following system of ordinary differential equations, similar to those found in, for example, Petrov and Pina (2010):

$$
\begin{aligned}
\frac{d}{dt}[A^-] &= \{-k_{-1}[A^-][H^+] + k_1[A]\} \\
\frac{d}{dt}[A] &= -\{-k_{-1}[A^-][H^+] + k_1[A]\} \\
&\quad + \{-k_{-2}[A][H^+] + k_2[AH^+]\} \\
\frac{d}{dt}[AH^+] &= -\{-k_{-2}[A][H^+] + k_2[AH^+]\} \\
&\quad + \{-k_3[AH^+] + k_{-3}[B][H^+]\} \\
\frac{d}{dt}[B] &= -\{-k_3[AH^+] + k_{-3}[B][H^+]\} \\
&\quad + \{-k_4[B] + k_{-4}[C]\} \\
&\quad + \{-k_6[B] + k_{-6}[B^-][H^+]\} \\
\frac{d}{dt}[B^-] &= -\{-k_6[B] + k_{-6}[B^-][H^+]\} \\
\frac{d}{dt}[C] &= -\{-k_4[B] + k_{-4}[C]\} \\
&\quad + \{-k_5[C] + k_{-5}[C^-][H^+]\} \\
\frac{d}{dt}[C^-] &= -\{-k_5[C] + k_{-5}[C^-][H^+]\}
\end{aligned} \tag{21}
$$

To find the steady-state concentrations, we first set all time derivatives to zero and represent all the concentrations in terms of $[A]$:

$$
\begin{aligned}
&[A^-] = \frac{K_1}{[H^+]}[A],\ [AH^+] = \frac{[H^+]}{K_2}[A],\ [B] = \frac{K_3}{K_2}[A], \\
&[B^-] = \frac{K_6K_3}{[H^+]K_2}[A],\ [C] = \frac{K_4K_3}{K2}[A], \\
&[C^-] = \frac{K_5K_4K_3}{K_2[H^+]}[A]
\end{aligned} \tag{22}
$$

The total anthocyanin concentration T is a conserved quality for the system (equation 21). In terms of the steady-state relations given by equation (22),

$$
\begin{aligned}
[T] &= [A^-] + [A] + [AH^+] + [B] \\
&\quad + [B^-] + [C] + [C^-] = K_T([H^+])[A]
\end{aligned} \tag{23}
$$

where

$$
\begin{aligned}
K_T([H^+]) &= \frac{K_1}{[H^+]} + 1 + \frac{[H^+]}{K_2} + \frac{K_3}{K_2} + \frac{K_6K_3}{[H^+]K_2} \\
&\quad + \frac{K_4K_3}{K_2} + \frac{K_5K_4K_3}{K_2[H^+]}
\end{aligned}
$$

The steady-state solution for $[A]$ is therefore

$$
[A] = \frac{[T]}{K_T([H^+])} \tag{24}
$$

Substituting this last expression into equation (22) yields the steady-state solutions for all species.

The steady-state solutions may therefore be graphed as functions of $\mathrm{pH} = -\log_{10}([H^+])$ for given values of the equilibrium constants $K_j = \frac{k_j}{k_{-j}} = 10^{-\mathrm{pK_j}}$, for $\mathrm{pK}_j = -\log_{10}(K_j)$. The values pK_j give the approximate pH values at which the species participating in the corresponding pair of reactions have equal concentrations at steady state. For example, the value pK_3 corresponding to the pair of reactions

$$
\mathrm{AH}^+ \underset{k_{-3}}{\overset{k_3}{\rightleftharpoons}} \mathrm{B}
$$

give the approximate pH value for which AH^+ and B have equal steady-state concentrations. The pK_j values for the anthocyanin malvidin 3,5-diglucsoside (malvin), found in Sadlowski (1985) and Moreira *et al.* (2003), have been measured to be $\mathrm{pK}_1 = 6.37$, $\mathrm{pK}_2 = 4$, $\mathrm{pK}_3 = 1.92$, $\mathrm{pK}_4 = 0.98$, $\mathrm{pK}_5 = 6.57$, and $\mathrm{pK}_6 = 7.86$. The steady-state concentrations of the

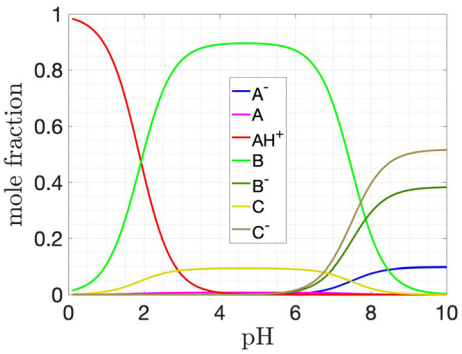

Figure 11. Equilibrium mole fractions of species of the anthocyanin malvin as a function of pH, as given by the steady-state solutions equations (22 and 24) to the system (equation 21). The equilibrium constants are those for malvin as described in the text, namely those corresponding to the pK values $pK_1 = 6.37$, $pK_2 = 4$, $pK_3 = 1.92$, $pK_4 = 0.98$, $pK_5 = 6.57$, and $pK_6 = 7.86$.

various species as functions of pH are shown in figure 11 using these pK_j values.

The results for malvin shown in figure 11 are in accordance with the description given earlier that, *of the colored species*, the red flavylium cation AH^+ dominates at low pH values, the purple species A dominates in the mid-range pH values, and the blue anion A^- dominates for high pH values. Strikingly, however, it is the colorless hemiketal B that has a much larger mole fraction than any colored species in the pH range 3–6, which includes the pH range of typical plant vacuoles. Association of anthocyanins with other molecules, as well as self association, whereby anthocyanin molecules form dimers, trimers, and larger *n*-mers affects the total concentration of colored species, as discussed in the following section.

4. Anthocyanin self association

In this section, we extend the anthocyanin speciation scheme given in section 3.2 to include self association. We begin in section 4.1 with an overview of association processes in anthocyanins, and analyze a mathematical model for self association in section 4.2.

4.1 *Overview of anthocyanin association*

Anthocyanin association occurs in a variety of ways. Intermolecular self association is characterized by interaction of two or more molecules of the same species (e.g. AH^+ with AH^+, A with A, or A^- with A^-) and cross reactions (AH^+ with A). We call an unassociated anthocyanin molecule a *monomer*. Two monomers can self associate to form a *dimer*; a monomer can associate with a dimer to form a *trimer*. In general, anthocyanin complexes formed by self association grow by monomer addition so that a monomer associates with an *n-1*-mer to form an *n*-mer consisting of *n* monomers. Intramolecular self association can occur by acyl function groups interacting with the chromophore within the same molecule (e.g. AH^+ with an acyl group). Association of anthocyanins also occurs with other, usually colorless, aromatic molecules called co-pigments (e.g. AH^+ with rutin). Interactions of all these associations occur by a combination of different bonding forces, e.g., dispersion-force $\pi-\pi$ stacking, hydrogen bonding of oxygen-containing functional groups (–OH, –C=O, –COOH, etc.) and ion dipole interactions. The strength and extent of association depends on the the following factors:

1. The structure of the chromophore; i.e., what substituent groups are attached to the A, B, and C rings. Anthocyanins with several hydroxyl groups in the B ring (such as delphinidin 3-glucoside) associate more strongly than other anthocyanins (such as pelargonidin 3-glucoside) (Gavara *et al.* 2013).
2. The charge type of a specific anthocyanin; i.e., whether the molecule exists in the form AH^+, A, A, A^-, or A^{2-}. Most of the *in vitro* experimental spectroscopic studies have been carried out on acidic aqueous solutions (pH <2) of the oxonium cation form (AH^+).
3. The nature and concentration of the counter ion. Again, most studies have been on the chlorides or perchlorates of AH^+ (AH^+CL^-, $AH^+CC_4{}^-$), although recently trifluoroacetate ion (CF_3COO^-) has been utilized.
4. The temperature. Although temperature is known to be a factor, few studies have been carried out. It is important, however, to understand that most plants undergo large day/night/weather temperature fluctuations (often as large as 40−50°C !).
5. The anthocyanin *concentration* appears to be the dominant factor. Again, most studies have been carried out on aqueous acidic solutions in the form AH^+X^-. Measured association constants range from 200 to 20000, and there appears to be significant association at concentrations greater than 10^{-3} M. It is important to express concentrations in units of mol·dm^{-3} since anthocyanin

molar masses range from about 400 mol·dm^{-3} to over 4000 mol·dm^{-3}. A fundamental problem in applying association concepts developed in aqueous acidic media is that the cell vacuolar environment is completely different. There are only a few studies of the vacuolar composition of flowers, in *Tulipa* and *Hippeastrum* (Wagner 1979), and in roses (Yamada *et al.* 2009). The problems associated with the use of spectroscopic techniques to measure *in vivo* molar anthocyanin concentrations include the difficulty of measuring vacuolar volumes, determining molar absorptivities, knowing vacuolar pH values, and understanding medium effects, since vacuoles contain relatively larger concentrations of, for example, fructose and glucose. Another interesting aspect of anthocyanin concentration is that the synthesis of pigments progresses as the flower progresses through various developmental stages. Two factors play a role, namely, the rate of anthocyanin production and the rate of increase of the cellular (vacuolar) volume. A good illustration of these processes is shown in the sequence of images of development of an orange geranium flower shown in the top panel of figure 12, where the increase in anthocyanin concentration can be seen. Images of the orange geranium epidermal edge cells of figure 12 show an increase in cell volume as the conical shape develops.

At concentrations above 10^{-3} M, the *n*-mers become large enough so that phase transitions can occur. The nucleation and growth characteristics of anthocyanin polymeric particulates are unknown. It is reasonable to assume that nanoparticles ($n > 100$) may form, followed by growth into larger pseudo-solid (and highly hydrated) particles. It is interesting to suggest that anthocyanins are amphiphiles and are chromogenic mesogens. The chromophores (the A, B, and C rings) are aromatic and hydrophobic (lipophilic), whereas the carbohydrate functional groups (monosaccharides,

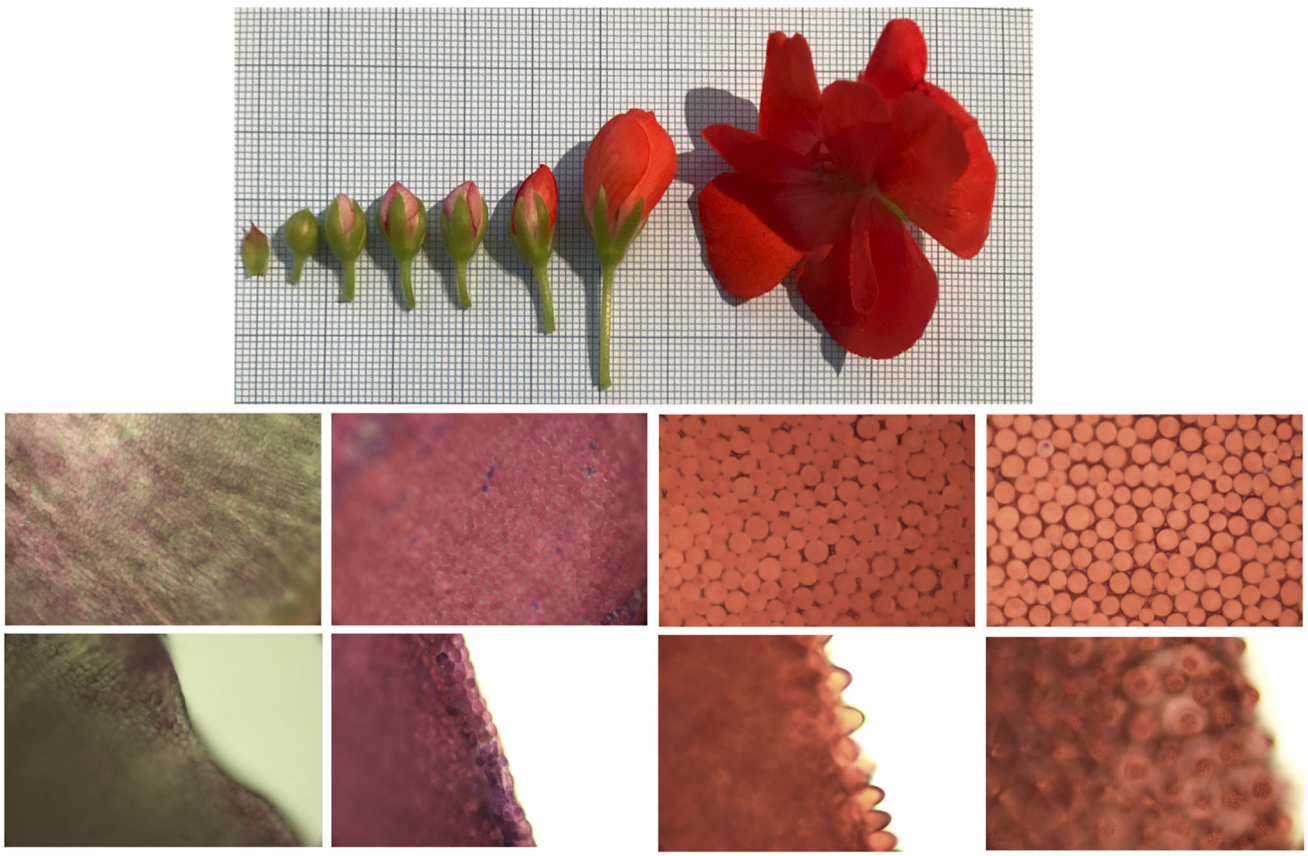

Figure 12. Top panel: Developmental sequence of an orange geranium flower, photographed on a 1 mm/1 cm square graph paper. Second and third rows: Developmental sequence of microscopic images of orange geranium epidermal cells seen looking down on the epidermis (second row, photographed at 20×) and from the side (third row, photographed at 40×). The sequence shows cells in the earlier (left) and later (right) stages of development.

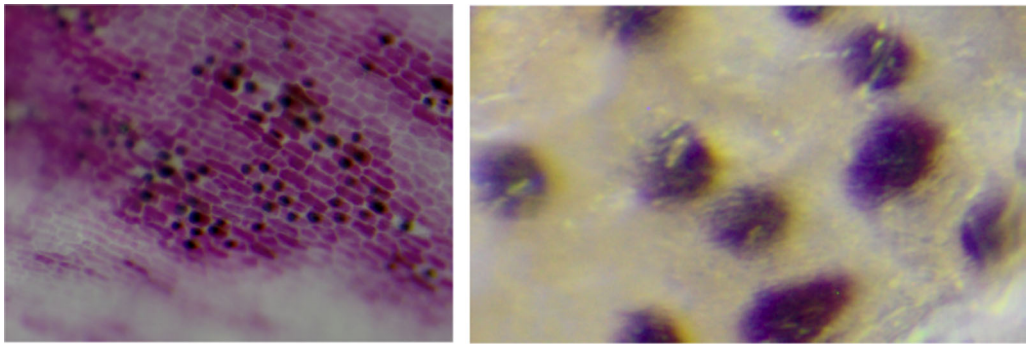

Figure 13. Microscopic images of epidermal cells of *Paeonia* (tree peony) flowers. Anthocyanic vacuolar inclusions are observed in many cells. The images were produced at 10× (left panel) and 40× (right panel) magnifications.

disaccharides, etc.) are hydrophilic (lipophobic). All anthocyanins are also chiral. This combination of structural factors gives rise to unusual and interesting new particulate properties. We are currenty studying these anthocyanin phase transitions by using designed evaporative techniques of aqueous flower extracts and *in vivo* peels of flowers, fruits, and vegetables. Microspectrometry (absorbance fluorescence), polarization analysis (for chirality), and surface property analysis (droplet contact angles) techniques are revealing fascinating new material properties of these mesogens.

One aspect of anthocyanin phase transitions that is receiving much attention is that of anthocyanic vacuolar inclusions (AVIs). These pseudo-solid bodies have been observed in the epiderms of flowers, fruits, and vegetables. A recent, elegant paper has shown that aromatic decoration of anthocyanins by acyl functional groups determine the formation of these vacuolar inclusions (Kallam *et al.* 2017). AVIs are good examples of phase transitions occurring at high concentrations of intramolecularly associated anthocyanins. We are currently studying a new example of AVI formation in the vacuole of tree peony (see figure 13).

4.2 *Kinetic equations and mathematical model for self association*

The following kinetic equations describe the process of self association by monomer addition to form *n*-mers up to a maximum size of *N*:

$$\begin{array}{lll} A^- + A^- \underset{j_{1,-2}}{\overset{j_{1,2}}{\rightleftharpoons}} (A^-)_2 & A + A \underset{j_{2,-2}}{\overset{j_{2,2}}{\rightleftharpoons}} (A)_2 & AH^+ + AH^+ \underset{j_{3,-2}}{\overset{j_{3,2}}{\rightleftharpoons}} (AH^+)_2 \\ A^- + (A^-)_2 \underset{j_{1,-3}}{\overset{j_{1,3}}{\rightleftharpoons}} (A^-)_3 & A + (A)_2 \underset{j_{2,-3}}{\overset{j_{2,3}}{\rightleftharpoons}} (A)_3 & AH^+ + (AH^+)_2 \underset{j_{3,-3}}{\overset{j_{3,3}}{\rightleftharpoons}} (AH^+)_3 \\ \vdots & \vdots & \vdots \\ A^- + (A^-)_{n-1} \underset{j_{1,-n}}{\overset{j_{1,n}}{\rightleftharpoons}} (A^-)_n & A + (A)_{n-1} \underset{j_{2,-n}}{\overset{j_{2,n}}{\rightleftharpoons}} (A)_n & AH^+ + (AH^+)_{n-1} \underset{j_{3,-n}}{\overset{j_{3,n}}{\rightleftharpoons}} (AH^+)_n \\ \vdots & \vdots & \vdots \\ A^- + (A^-)_{N-1} \underset{j_{1,-N}}{\overset{j_{1,N}}{\rightleftharpoons}} (A^-)_N & A + (A)_{N-1} \underset{j_{2,-N}}{\overset{j_{2,N}}{\rightleftharpoons}} (A)_N & AH^+ + (AH^+)_{N-1} \underset{j_{3,-N}}{\overset{j_{3,N}}{\rightleftharpoons}} (AH^+)_N \end{array} \tag{25}$$

(26)

There is also evidence for association of A with AH^+ as given by the following set of reactions (Hoshino 1991, 1992)

$$
\begin{aligned}
&A + AH^+ \underset{j_{4,-2}}{\overset{j_{4,2}}{\rightleftharpoons}} A \cdot AH^+ \\
&AH^+ + A \cdot AH^+ \underset{j_{4,-3}}{\overset{j_{4,3}}{\rightleftharpoons}} A \cdot (AH^+)_2 \\
&A + A \cdot (AH^+)_2 \underset{j_{4,-4}}{\overset{j_{4,4}}{\rightleftharpoons}} (A)_2 \cdot (AH^+)_2 \\
&AH^+ + (A)_2 \cdot (AH^+)_2 \underset{j_{4,-5}}{\overset{j_{4,5}}{\rightleftharpoons}} (A)_2 \cdot (AH^+)_3 \\
&\qquad\qquad \vdots \\
&A + (A)_{\frac{N}{2}-1} \cdot (AH^+)_{\frac{N}{2}} \underset{j_{4,-N}}{\overset{j_{4,N}}{\rightleftharpoons}} (A)_{\frac{N}{2}} \cdot (AH^+)_{\frac{N}{2}}
\end{aligned} \tag{27}
$$

Combining the speciation scheme as given by equation 20 with self association as given by these kinetic equations yields the following system of differential equations: For monomers $[A^-]$ of the anhydrous base and its n-mers $[(A^-)_n]$,

$$
\begin{aligned}
\frac{d}{dt}[A^-] &= \{-k_{-1}[A^-][H^+] + k_1[A]\} \\
&\quad + 2\{-j_{1,2}[A^-][A^-] + j_{1,-2}[(A^-)_2]\} \\
&\quad + \{-j_{1,3}[A^-][(A^-)_2] + j_{1,-3}[(A^-)_3]\} \\
&\quad + \cdots + \{-j_{1,N}[A^-][(A^-)_{N-1}] \\
&\quad + j_{1,-N}[(A^-)_N]\} \\
\frac{d}{dt}[(A^-)_2] &= -\{-j_{1,2}[A^-][A^-] + j_{1,-2}[(A^-)_2]\} \\
&\quad + \{-j_{1,3}[A^-][(A^-)_2] + j_{1,-3}[(A^-)_3]\} \\
&\quad \vdots \\
\frac{d}{dt}[(A^-)_N] &= -\{-j_{1,N}[A^-][(A^-)_{N-1}] \\
&\quad + j_{1,-N}[(A^-)_N]\}
\end{aligned} \tag{28}
$$

The kinetic equations for the monomers $[A]$ of the quinoidal base and its n-mers $[(A)_n]$ couple with those for the monomers $[AH^+]$ of the flavylium cation and its n-mers $[(AH^+)_n]$ due to the complexes formed from mixtures of these species. The kinetic equations read as

$$
\begin{aligned}
\frac{d}{dt}[A] &= -\{-k_{-1}[A^-][H^+] + k_1[A]\} \\
&\quad + \{-k_{-2}[A][H^+] + k_2[AH^+]\} \\
&\quad + 2\{-j_{2,2}[A][A] + j_{2,-2}[(A)_2]\} \\
&\quad + \{-j_{2,3}[A][(A)_2] + j_{2,-3}[(A)_3]\} \\
&\quad + \cdots + \{-j_{2,N}[A][(A)_{N-1}] + j_{2,N}[(A)_N]\} \\
&\quad + \{-j_{4,2}[A][AH^+] + j_{4,-2}[A \cdot AH^+]\} \\
&\quad + \{-j_{4,4}[A][A \cdot (AH^+)_2] + j_{4,-4}[(A)_2 \\
&\quad \cdot (AH^+)_2]\} \\
&\quad + \cdots + \{-j_{4,N}[A][(A)_{\frac{N}{2}-1} \cdot (AH^+)_{\frac{N}{2}}] \\
&\quad + j_{4,-N}[(A)_{\frac{N}{2}} \cdot (AH^+)_{\frac{N}{2}}]\} \\
\frac{d}{dt}[(A)_2] &= -\{-j_{2,2}[A][A] + j_{2,-2}[(A)_2]\} \\
&\quad + \{-j_{2,3}[A][(A)_2] + j_{2,-3}[(A)_3]\} \\
&\quad \vdots \\
\frac{d}{dt}[(A)_N] &= -\{-j_{2,N}[A][(A)_{N-1}] + j_{2,N}[(A)_N]\}
\end{aligned} \tag{29}
$$

for the n-mers $[(A)_n]$,

$$
\begin{aligned}
\frac{d}{dt}[AH^+] &= -\{-k_{-2}[A][H^+] + k_2[AH^+]\} \\
&\quad + \{-k_3[AH^+] + k_{-3}[B][H^+]\} \\
&\quad + 2\{-j_{3,2}[AH^+][AH^+] + j_{3,-2}[(AH^+)_2]\} \\
&\quad + \{-j_{3,3}[AH^+][(AH^+)_2] + j_{3,-3}[(AH^+)_3]\} \\
&\quad + \cdots + \{-j_{3,N}[AH^+][(AH^+)_{N-1}] \\
&\quad + j_{3,N}[(AH^+)_N]\} \\
&\quad + \{-j_{4,2}[A][AH^+] + j_{4,-2}[A \cdot AH^+]\} \\
&\quad + \{-j_{4,3}[A \cdot AH^+][AH^+] + j_{4,-3}[A \cdot (AH^+)_2]\} \\
&\quad + \cdots + \{-j_{4,N-1}[(A)_{\frac{N}{2}-1} \cdot (AH^+)_{\frac{N}{2}-1}][AH^+] \\
&\quad + j_{4,-(N-1)}[(A)_{\frac{N}{2}-1} \cdot (AH^+)_{\frac{N}{2}}]\} \\
\frac{d}{dt}[(AH^+)_2] &= -\{-j_{3,2}[AH^+][AH^+] \\
&\quad + j_{3,-2}[(AH^+)_2]\} \\
&\quad + \{-j_{3,3}[AH^+][(AH^+)_2] + j_{3,-3}[(AH^+)_3]\} \\
&\quad \vdots \\
\frac{d}{dt}[(AH^+)_N] &= -\{-j_{3,N}[AH^+][(AH^+)_{N-1}] \\
&\quad + j_{3,-N}[(AH^+)_N]\}
\end{aligned} \tag{30}
$$

for the n-mers $[(AH^+)_n]$, and

$$\begin{aligned}
\frac{d}{dt}[A\cdot AH^+] &= -\{-j_{4,2}[A][AH^+]+j_{4,-2}[A\cdot AH^+]\}\\
&\quad+\{-j_{4,3}[A\cdot AH^+][AH^+]\\
&\quad+j_{4,-3}[A\cdot (AH^+)_2]\}\\
\frac{d}{dt}[A\cdot (AH^+)_2] &= -\{-j_{4,3}[A\cdot AH^+][AH^+]\\
&\quad+j_{4,-3}[A\cdot (AH^+)_2]\}\\
&\quad+\{-j_{4,4}[A][A\cdot (AH^+)_2]\\
&\quad+j_{4,-4}[(A)_2\cdot (AH^+)_2]\}\\
\frac{d}{dt}[(A)_2\cdot (AH^+)_2] &= -\{-j_{4,4}[A][A\cdot (AH^+)_2]\\
&\quad+j_{4,-4}[(A)_2\cdot (AH^+)_2]\}\\
&\quad+\{-j_{4,5}[(A)_2\cdot (AH^+)_2][AH^+]\\
&\quad+j_{4,-5}[(A)_2\cdot (AH^+)_3]\}\\
&\quad\vdots\\
\frac{d}{dt}[(A)_{\frac{N}{2}}\cdot (AH^+)_{\frac{N}{2}}] &= -\{-j_{4,N}[A][(A)_{\frac{N}{2}-1}\\
&\quad\cdot (AH^+)_{\frac{N}{2}}]+j_{4,-N}[(A)_{\frac{N}{2}}\\
&\quad\cdot (AH^+)_{\frac{N}{2}}]\}
\end{aligned}\tag{31}$$

for the n-mers $(A)_n\cdot(AH^+)_n$ and $(A)_n\cdot(AH^+)_{n+1}$. These kinetic equations couple with the kinetic equations of the remaining species, $[B]$, $[B^-]$, $[C]$, and $[C^-]$, that do not undergo self association, namely,

$$\begin{aligned}
\frac{d}{dt}[B] &= -\{-k_3[AH^+]+k_{-3}[B][H^+]\}\\
&\quad+\{-k_4[B]+k_{-4}[C]\}+\{-k_6[B]\\
&\quad+k_{-6}[B^-][H^+]\}\\
\frac{d}{dt}[B^-] &= -\{-k_6[B]+k_{-6}[B^-][H^+]\}\\
\frac{d}{dt}[C] &= -\{-k_4[B]+k_{-4}[C]\}\\
&\quad+\{-k_5[C]+k_{-5}[C^-][H^+]\}\\
\frac{d}{dt}[C^-] &= -\{-k_5[C]+k_{-5}[C^-][H^+]\}
\end{aligned}\tag{32}$$

The final system of equations including anthocyanin speciation and self association is given by equations (29), (30), (31), and (32). This system of equations, similar to those found in, for example, Leydet *et al.* (2012), satisfies the conservation law

$$\begin{aligned}
T = {} & [B]+[B^-]+[C]+[C^-]+\sum_{n=1}^{N}\{n[(A^-)_n]\\
&+n[(A)_n]+n[(AH^+)_n]\}\\
&+\sum_{n=1}^{N/2-1}(2n+1)[(A)_n\cdot(AH^+)_{n+1}]\\
&+\sum_{n=1}^{N/2}2n[(A)_n\cdot(AH^+)_n]
\end{aligned}\tag{33}$$

As for the equations of section 3.2, in which we only included anthocyanin speciation, we find the steady-state concentrations by first solving for all concentrations in terms of the concentration of the anhydrous base $[A]$ and then applying the conservation law for the total anthocyanin concentration T. This yields again the solutions (equation 22) for the monomer concentrations. For simplicity, we also make the *isodesmic* assumption that the equilibrium constants for association are independent of n; that is, for all n,

$$\begin{aligned}
J_1 = J_{1,n} = \frac{j_{1,n}}{j_{1,-n}}, \quad J_2 = J_{2,n} = \frac{j_{2,n}}{j_{2,-n}}\\
J_3 = J_{3,n} = \frac{j_{3,n}}{j_{3,-n}}, \quad J_4 = J_{4,n} = \frac{j_{4,n}}{j_{4,-n}}
\end{aligned}\tag{34}$$

Given this assumption of isodesmicity, the concentrations of the associated species as functions of $[A]$ are given by

$$\begin{aligned}
[(A^-)_n] &= \frac{1}{J_1}\left(\frac{J_1K_1}{[H^+]}\right)^n[A]^n\\
[(A)_n] &= J_2^{n-1}[A]^n, \quad [(AH^+)_n] = \frac{1}{J_3}\left(\frac{J_3[H^+]}{K_2}\right)^n[A]^n\\
[(A)_n\cdot(AH^+)_{n+1}] &= (J_4)^{2n}\left(\frac{[H^+]}{K_2}\right)^{n+1}[A]^{2n+1}\\
[(A)_n\cdot(AH^+)_n] &= (J_4)^{2n-1}\left(\frac{[H^+]}{K_2}\right)^{n}[A]^{2n}
\end{aligned}\tag{35}$$

Substituting these steady-state solutions into the conservation law given by equation (33) yields a polynomial equation of degree N in [A]. This equation has the form

$$p([A]) = q([A]) - T = 0\tag{36}$$

where $q([A])$ is a polynomial in $[A]$ for which $q(0) = 0$ but all coefficients of powers of $[A]$ larger than 0 are positive. Therefore, $p(0) = -T$, but $p([A])$ is a strictly

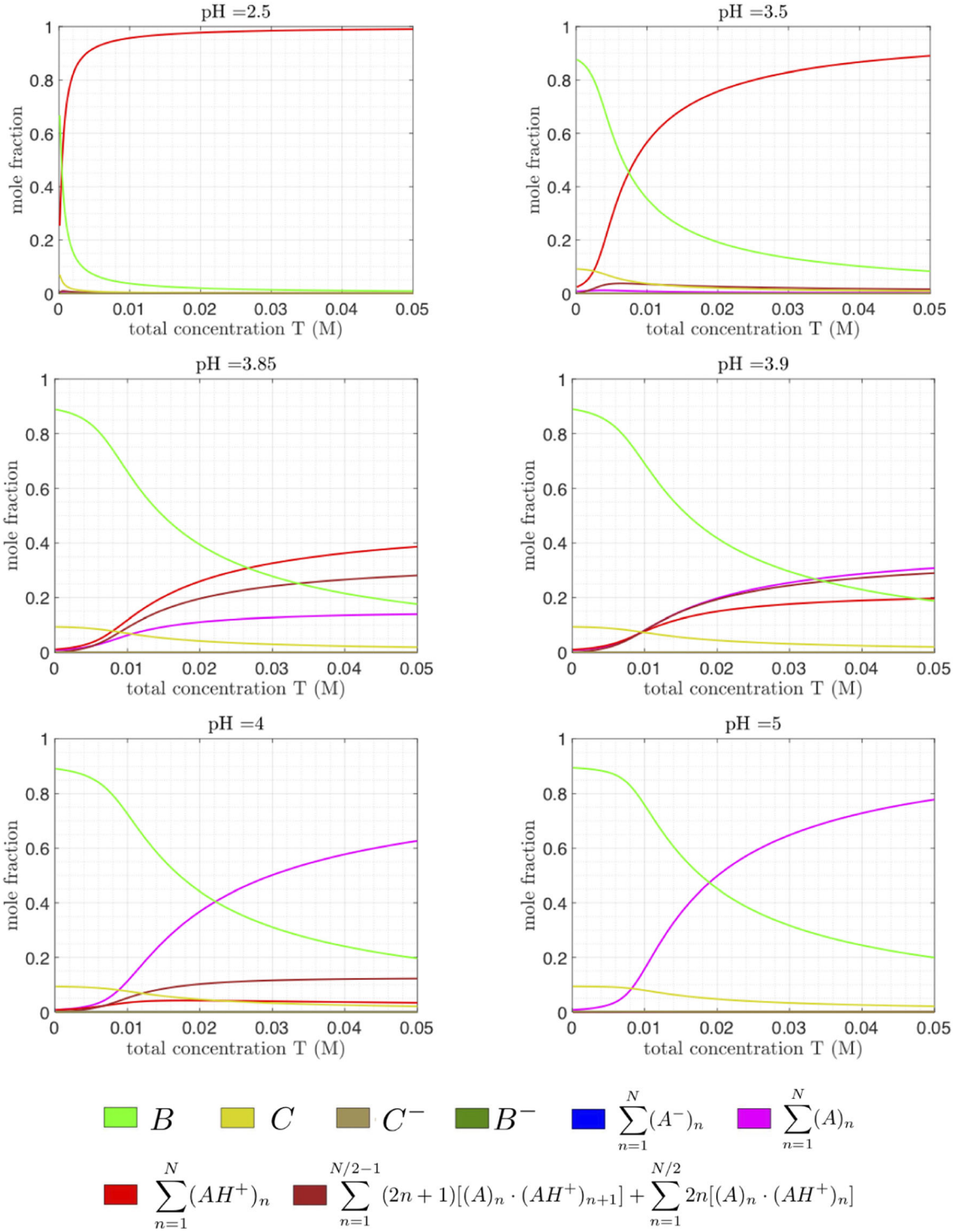

Figure 14. Steady-state mole fractions of anthocyanin species as a function of total anthocyanin concentration T. The steady-state solutions to the system given by equations (29), (30), and (32), are given by equations (22) and (35), assuming the isodesmic model as described in the text. The equilibrium constants are measured values for the anthocyanin malvin (pK values $pK_1 = 6.37$, $pK_2 = 4$, $pK_3 = 1.92$, $pK_4 = 0.98$, $pK_5 = 6.57$, and $pK_6 = 7.86$), and for the equilibria of self association these are $J_1 = 3200$, $J_2 = 12,800$, and $J_3 = 9600$, and $J_4 = 11,200$, based on measurements of Hoshino (1992). We chose $N = 20$ as the maximum size of the associated species for these calculations.

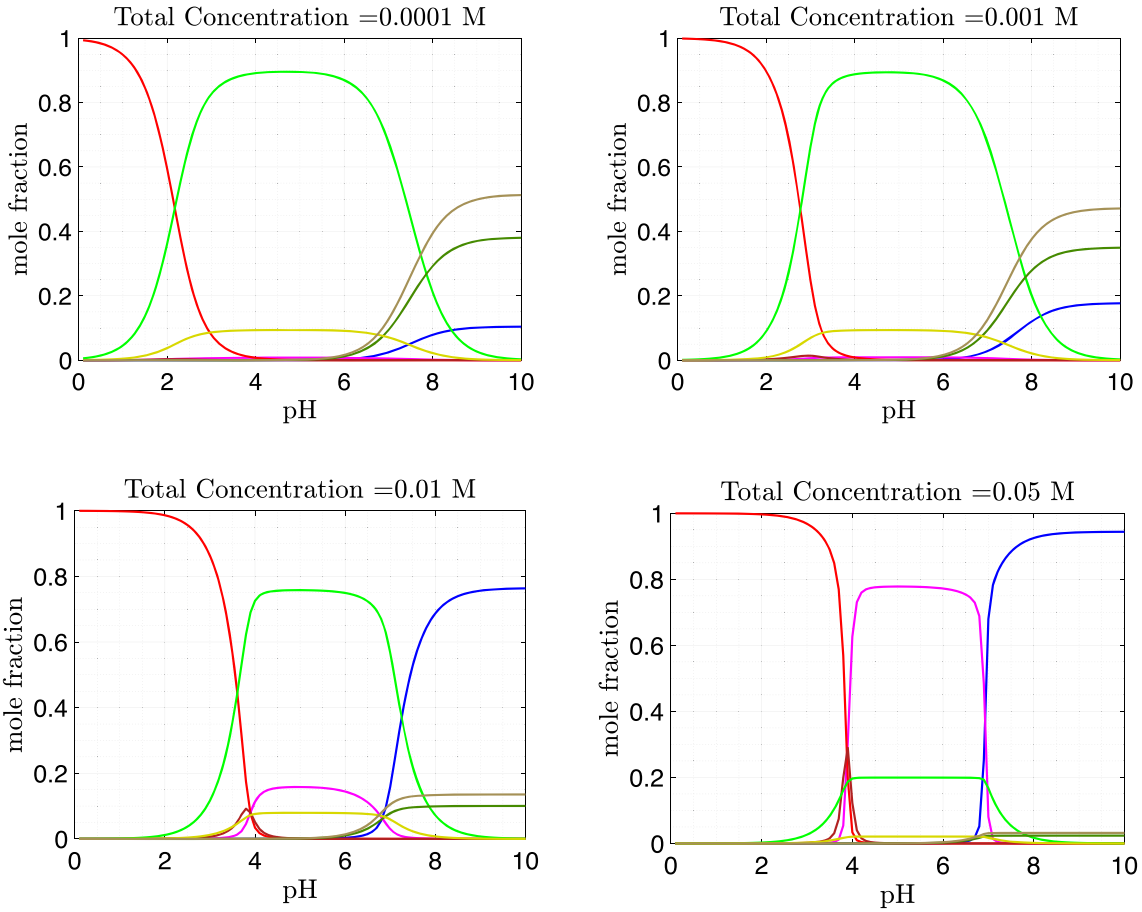

Figure 15. Equilibrium mole fractions of species of the anthocyanin malvin as a function of pH. The steady-state solutions to the system given by equations (29), (30), and (32) are given by equations (22) and (35), assuming the isodesmic model as described in the text and the parameter values given in the caption to figure 14. The color coding is the same as for the legend to figure 14.

increasing function of $[A]$ for $[A] > 0$; the polynomial $p([A])$ has a unique positive root.

Graphs of the mole fractions of the various species as functions of the total anthocyanin concentration T are shown in figure 14 for six different choices of the pH value. The equilibrium constants for association were chosen as $J_1 = 3200, J_2 = 12,800, J_3 = 9600, J_4 = 11,200$, based on measurements for malvin by Hoshino (1992). The plots of figure 14 demonstrate a key feature of self association: *as total concentration T increases, the mole fraction of the species that self associate increases.* Since the species that undergo self association are the *colored* species A^-, A, and AH^+, self association increases the mole fraction of colored species. This increase in colored species depends on the pH value, but generally is dramatic indeed. Observe, for example, that at a pH of 3.5, the colorless hemiketal B is the dominant species if the total concentration is lower than 0.007, whereas the sum of the AH^+ *n*-mers enjoy a mole fraction of nearly 0.9 if the total concentration is 0.05 M. Analogous plots to those in figure 14 but showing the mole fractions of the species as functions of pH for four fixed values of the total concentration T are shown in figure 15. In particular, note that the mole fraction of the purple species $(A)_n$ in the pH range 4–6 is nearly zero for $T < 10^{-3}$ M, but then increases nonlinearly as a function of the total concentration.

These results suggest a reason that colored pigments are observed in plant cell vacuoles despite the pH range of 3–6 that favors the colorless species (figure 11): For high enough total anthocyanin concentrations, self association of the colored species pulls the equilibrium towards a state with a large mole fraction of those colored species. With this in mind, return to the purple *S. yangii* stripe flanked by white cells as pictured in figure 4(d). The cells in the center of the stripe likely have large enough anthocyanin concentrations so that self association can induce a large mole fraction of the

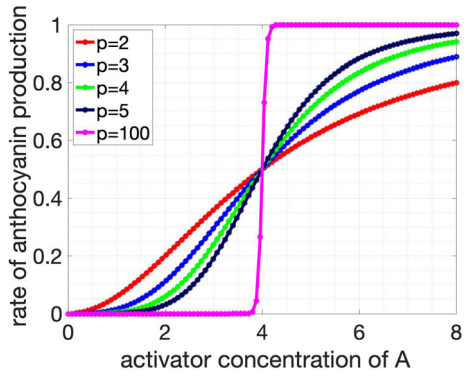

Figure 16. The sigmoidal relationship given by equation (37) represents the dependence of the activator production rate on activator concentration. The threshold parameter in equation (37) is chosen to be $\tau = 4$, and the relation is shown for various values of the power p.

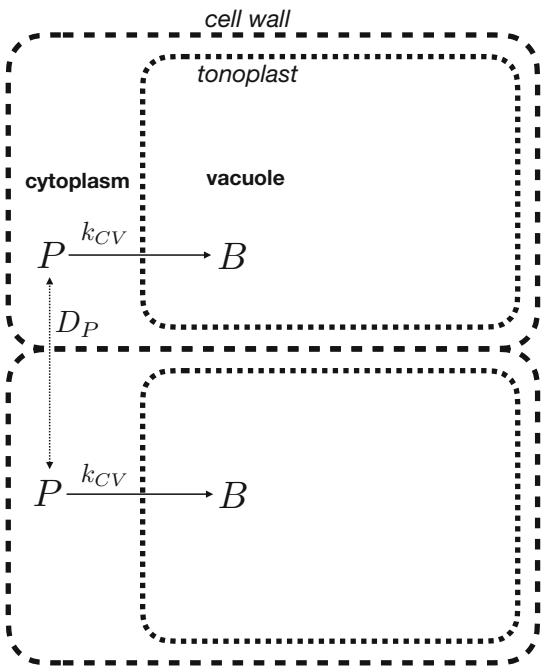

Figure 17. Schematic diagram of two adjacent plant cells and processes of anthocyanin transport and diffusion. Anthocyanins are synthesized in the cytoplasm, where the pH is approximately 7 and are transported across the tonoplast membrane to the vacuole, where the pH ranges from 3 to 6, or possibly diffuse or are transported between the cytoplasms of adjacent cells.

colored species A at the typical vacuolar pH range of 3–6. The white cells might initially appear to not contain anthocyanins. However, as demonstrated in figure 4(e), the diffusion of HCl vapor across the surface of the epidermis, thereby lowering the pH of the cells, turns the purple cells red as expected according to the speciation kinetics. But, this process also induces a fainter red color in the white cells. This indicates that anthocyanins are present all along even in the white cells, but at a low enough concentration so that they are primarily in the colorless hemiketal or chalcone forms. Only when the pH is lowered, does one observe the anthocyanins as (red) colored species, in accordance with the plots shown in figure 15.

Therefore there can be more to an anthocyanin pattern than meets the eye: Anthocyanins may be present even in regions that lack their signature blue, purple, and red colors. This realization motivates us to extend the activator–inhibitor model proposed by Ding *et al.* (2020) to consider how variation in total anthocyanin concentration couples with speciation and association.

5. Activation-inhibition coupled to speciation and self association

In this section, we extend the activator–inhibitor model of Ding *et al.* as reviewed and analyzed in section 2 to include (i) anthocyanin synthesis, diffusion, and transport from the cytoplasm to the vacuole, (ii) anthocyanin speciation (as described in section 3), and (iii) anthocyanin self association (as described and combined with speciation in section 4).

5.1 *Anthocyanin synthesis*

The model presented by Ding *et al.* makes the simple assumption that anthocyanin is present at the spatial positions where the activator exceeds a threshold value. To couple anthocyanin synthesis to the kinetics of speciation and self association, we first incorporate a rate of anthocyanin synthesis that depends on the activator concentration. The rate of anthocyanin synthesis is an increasing function of activator concentration. The synthesis rate of a protein typically follows a sigmoidal relationship with respect to activator concentration (Veitia 2003). We employ using a Hill function sigmoidal relationship of the form

$$u_{act}(A; p, \tau) = \frac{A^p}{A^p + \tau^p} \tag{37}$$

The parameter τ is a threshold value of an activator below (above) which the production rate of anthocyanin is small (large). Larger values of p produce a more pronounced jump from low to high synthesis rate as the concentration of activator increases above τ. Veitia (2003) points out that if the activator concentration is half of τ, the synthesis rate is small. The

power p should be large enough to incorporate this observation (figure 16).

5.2 *Anthocyanin diffusion and transport*

Anthocyanin molecules are synthesized in the cytoplasm, where the typical pH is approximately equal to 7. At this pH value and at low concentrations, we expect the synthesized anthocyanins to be present as colorless precursor species (for example, chalcones and hemiketal forms; see figure 11). We therefore assume that anthocyanin molecules in the cytoplasm are all in a colorless precursor form and denote anthocyanins in the cytoplasm by P. These molecules move in two ways as schematized in figure 17: First, they may diffuse between cells. Second, in each cell, they are transported from the cytoplasm across the tonoplast into the vacuole of that cell (Poustka *et al.* 2007; Sun *et al.* 2012; Chanoca *et al.* 2015). The anthocyanin molecules that are transported into the vacuole are initially in a precursor form that may be the hemiketal or the chalcone. We denote these molecules by P. The pH range of a typical plant cell vacuole is 3–6; thus, the precursor anthocyanin P molecules that are transported to the vacuole experience a pH shift. We assume these molecules arrive in the vacuole in the hemiketal form and therefore denote them by B. These molecules may undergo the pH-dependent speciation and self association reactions described by the model in section 4. The anthocyanin molecules in a cell's vacuole are, however, confined to that cell. Therefore, we do not include any diffusion of these molecules.

The partial differential equations that govern the diffusing species are as follows:

$$\frac{\partial A}{\partial t} = D_A \cdot \triangle A + G_A \frac{A^2 + A_0}{I + K} - U_A \cdot A \tag{38}$$

$$\frac{\partial I}{\partial t} = D_I \cdot \triangle I + G_I \cdot A^2 + I_0 - U_I \cdot I \tag{39}$$

$$\frac{\partial P}{\partial t} = D_P \cdot \triangle P + \gamma u_{act(n,thr)}(A) - \delta P - \tau_{CV} P \tag{40}$$

where τ_{CV} is the rate constant for anthocyanin transport from the cytoplasm to the vacuole, and the parameter of synthesis potency γ is the maximum rate constant for anthocyanin synthesis. The rate of change of the concentration of the hemiketal B in the vacuole is

$$\begin{aligned}\frac{d}{dt}[B] = {} & \tau_{CV} P - \delta[B] \\ & - \{-k_3[AH^+] + k_{-3}[B][H^+]\} \\ & + \{-k_4[B] + k_{-4}[C]\} + \{-k_6[B] \\ & + k_{-6}[B^-][H^+]\}\end{aligned} \tag{41}$$

We assume that all anthocyanin species in the cytoplasm or the vacuole degrade with rate constant δ. The remaining equations in our final model system therefore consist of equations (28) to (32), with the addition of $-\delta[\bullet]$ in each equation for species $\bullet$ in the vacuole. In all simulations, we use the prototypical set of parameter values for the activator–inhibitor system, along with the following parameter values: the diffusion coefficient for anthocyanin in the cytoplasm $D_B = 10^{-2}$; the speciation kinetic rate constants $k_1 = 3 \times 10^{3.2}, k_{-1} = 3 \times 10^{10}, k_2 = 3 \times 10^6, k_{-2} = 3 \times 10^{10}$, $k_3 = 0.2849, k_{-3} = 23.7, k_4 = 3 \times 10^5, k_{-4} = 3 \times 10^{5.98}$, $k_5 = 3 \times 10^{3.25}$, $k_{-5} = 3 \times 10^{10}, k_6 = 3 \times 10^{2.14}$, $k_{-6} = 3 \times 10^{10}$; the rate constants for association $j_{1,n} = j_{2,n} = j_{3,n} = j_{4,n} = 8000$ and $J_1 = 3200, J_2 = 12,800, J_3 = 9600, J_4 = 11,200$; the sigmoidal response power $p = 4$ with the threshold constant $\tau = 4$ and synthesis potency $\gamma = 5 \times 10^{-4}$, the transport rate constant $\tau_{CV} = 5 \times 10^{-5}$, and the degradation rate constant $\delta = 10^{-2}$.

Figures 18, 19, and 20 show distributions of anthocyanin species in the vacuole resulting from numerical simulations of our final model system to time $t = 2.5 \cdot 10^5$, at pH values of 3.7 (figure 18 and figure 20(a,b)) and 5 (figure 19, figure 20(c,d)). The parameter U_I was chosen to be $U_I = 0.2564$, so that the dimensionless bifurcation parameter has the value $Q = 0.82\ Q_T \simeq 7.0084$. The remaining parameters are as listed in the previous paragraph. The left (right) columns of figures 18 and 19 show the species distributions at the positions of minimal (maximal) activator concentration. The total anthocyanin concentration in the cell vacuoles at the position of minimum activator concentration is $9.4 \cdot 10^{-3}$ M, whereas it is $3.89 \cdot 10^{-2}$ M at the position of maximum activator concentration. As shown in the pie graphs in the first rows of figures 18 and 19, the majority of the anthocyanin is in a colorless hemiketal or chalcone form at the minimum concentration for either pH value. At the maximum concentration, however, over 80% of the anthocyanin is a colored form (mostly AH^+ at pH 3.7

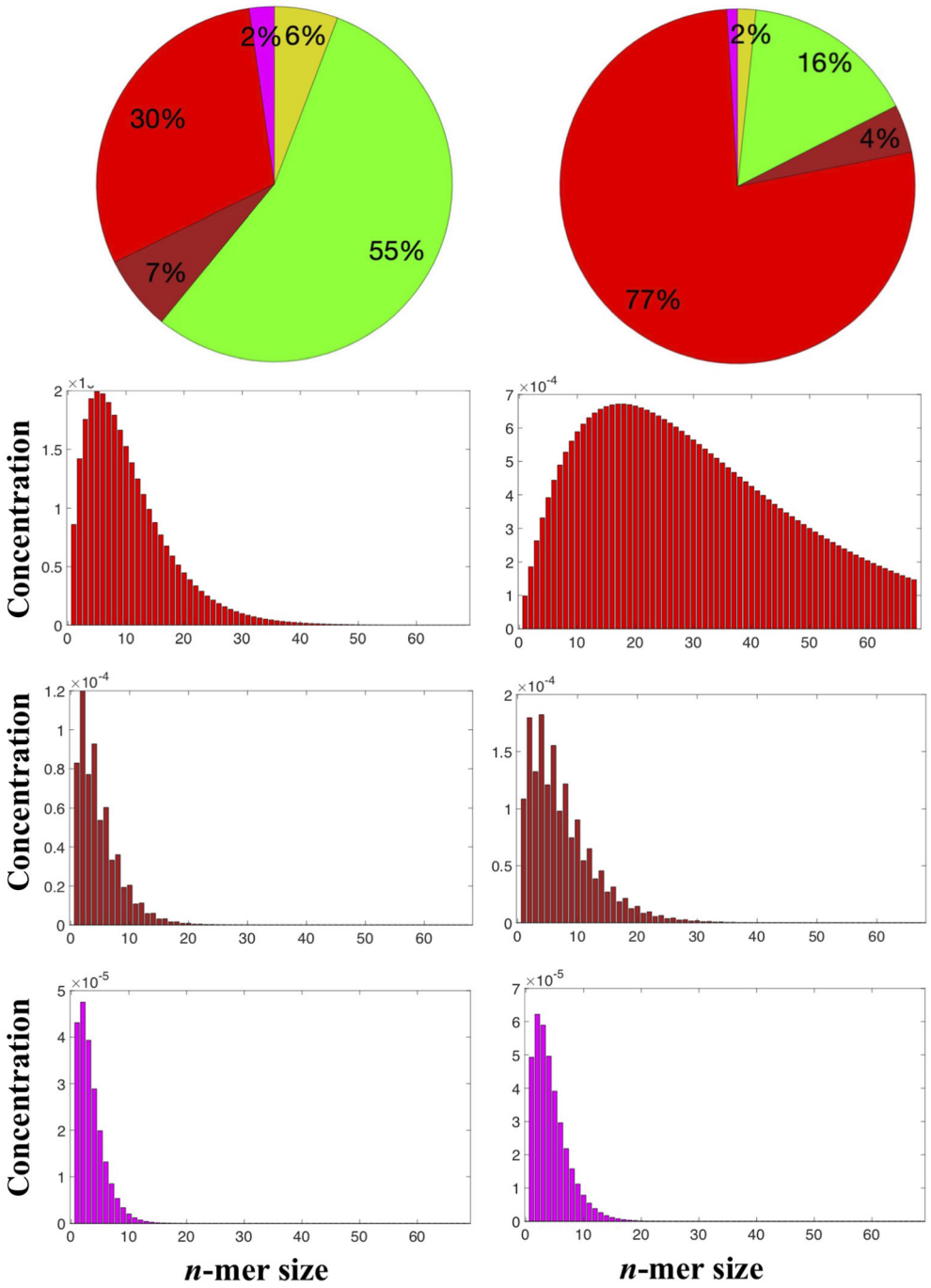

Figure 18. Anthocyanin species distributions at spatial positions of minimal (left column) and maximal (right column) activator concentrations at pH 3.7. The distributions result from numerical simulations of the final model system to time $t = 2.5 \times 10^5$ with the parameter values described in the text. At positions of minimal (maximal) activator concentrations, the total anthocyanin concentration in the vacuole was 9.4×10^{-3} (3.89×10^{-2}). The pie graphs in the first row show the distributions of the total sum of all n-mers for a given anthocyanin species; the color coding is given in the legend to figure 14, and the species percentages are given for species that make up more than 1% of the total. In the bottom three rows are plotted $[(AH^+)_n]$ (first row), $[(A)_n \cdot (AH^+)_n]$ (second row) and (A_n) (third row) vs. n at the positions of minimal (left column) and maximal (right column) activator concentrations.

and mostly A at pH 5). This is in agreement with the results of section 4. The bottom three rows of figures 18 and 19 show the size distributions of associated anthocyanin molecules in the colored forms. These plots show the concentrations of the various n-mers as functions of n. Larger concentrations increase

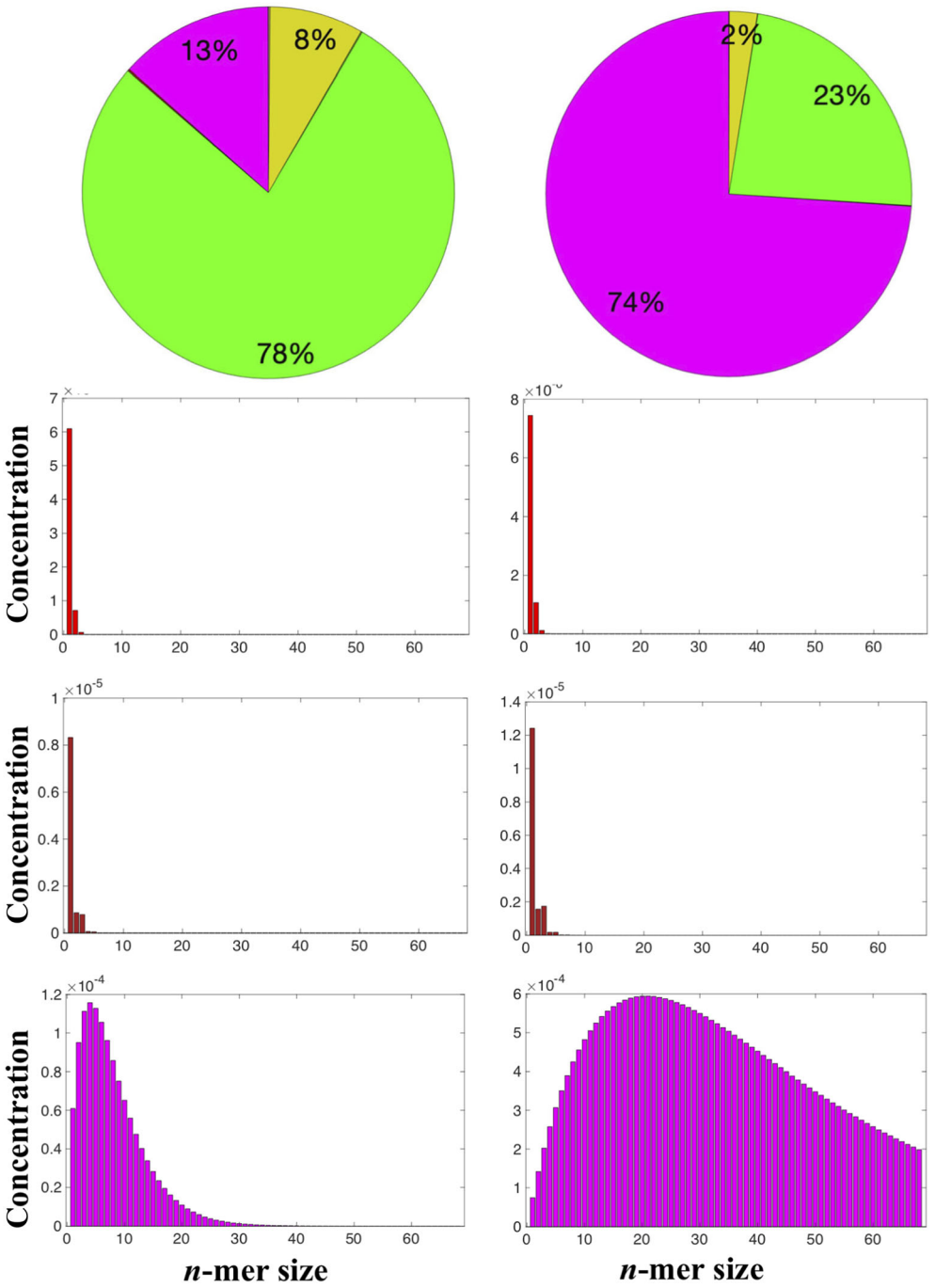

Figure 19. Anthocyanin species distributions at spatial positions of minimal (left column) and maximal (right column) activator concentrations at pH 5. The distributions result from numerical simulations of the final model system to time $t = 2.5 \times 10^5$ with the parameter values described in the text. At positions of minimal (maximal) activator concentrations, the total anthocyanin concentration in the vacuole was 9.4×10^{-3} (3.89×10^{-2}). The pie graphs in the first row show the distributions of the total sum of all n-mers for a given anthocyanin species; the color coding is given in the legend to figure 14, and the species percentages are given for species that make up more than 1% of the total. In the bottom three rows are plotted $[(AH^+)_n]$ (first row), $[(A)_n \cdot (AH^+)_n]$ (second row) and (A_n) (third row) vs. n at the positions of minimal (left column) and maximal (right column) activator concentrations.

the mean size of an associated molecule, so that monomers dominate at low concentrations, whereas larger n-mers dominate at higher concentrations.

Aspects of these species distributions as they vary spatially across the two-dimensional patterns appear in figure 20. For the pH values 3.7 and 5 respectively,

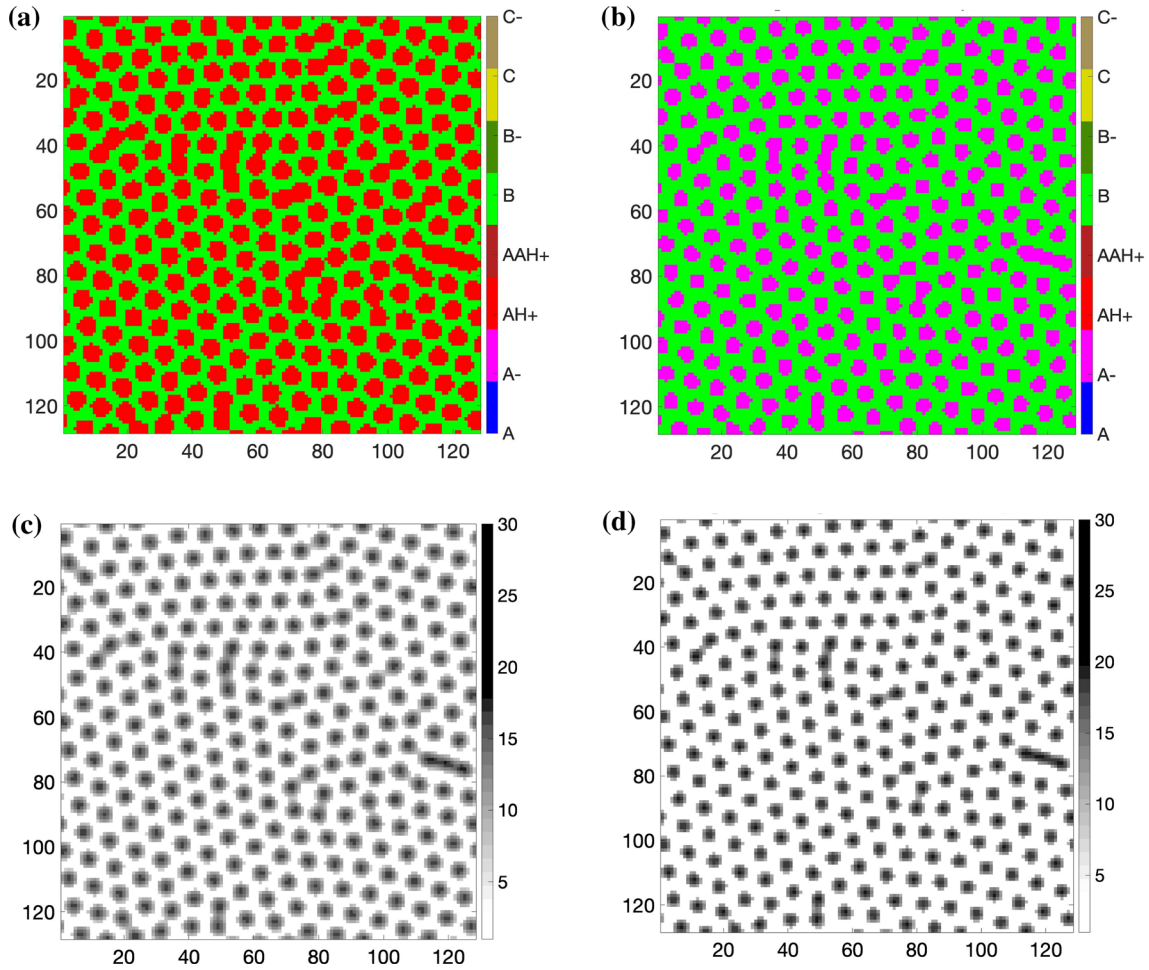

Figure 20. Two-dimensional patterns resulting from numerical simulations of the final model system to time $t = 2.5 \times 10^5$ with the parameter values described in the text. For panels (**a**) and (**c**), the pH is 3.7, whereas for panels (**b**) and (**d**), the pH is 5. Panels (**a**) and (**b**) show which species has the largest concentration at any position in space, as indicated in the side-bar legend. We call that species as the *dominant species* at that position. The concentrations of the species that undergo self association are calculated as the sum over all *n*-mers of that species. Panels (**c**) and (**d**) plot show, as a function of the spatial position, which *n*-mer of the dominant species at that position has the largest concentration, as indicated by the side-bar legend.

panels (a) and (b) of this figure indicate which species has the largest concentration at any spatial position. The colored species appear in a spot pattern similar to patterns produced by the model of Ding *et al.* (2020), which resemble patterns on monkeyflowers. A comparison of the patterns produced at the pH values 3.7 and 5 yields an interesting observation: The spots are larger for the pattern produced at pH 3.7 than for pattern produced at pH 5. This is the case even though all other parameter values, including the parameter U_I that is a focus of Ding *et al.* (2020), are the same for both cases. In figure 20(c,d) we plot, as a function of the spatial position, which *n*-mer of the dominant species at that position has the largest concentration. The centers of the colored regions are characterized by a higher degree of association.

Similarly, figure 21 illustrates aspects of a two-dimensional pattern with pH equal to 5 and otherwise the same parameter values as for figures 18, 19, and 20, except that $U_I = 0.2103$, so that $Q = 0.9725\, Q_T \approx 8.3118$. This simulation results in a stripe pattern that alternates between regions dominated by the purple A species and the colorless hemiketal B, as shown in panel (a). The model predicts that the A species has its largest concentration (as shown by the cross section plotted in panel (c)) as well as highest degree of association (as shown in panel (b) and the cross section plotted in panel (d)) in the center of the stripes.

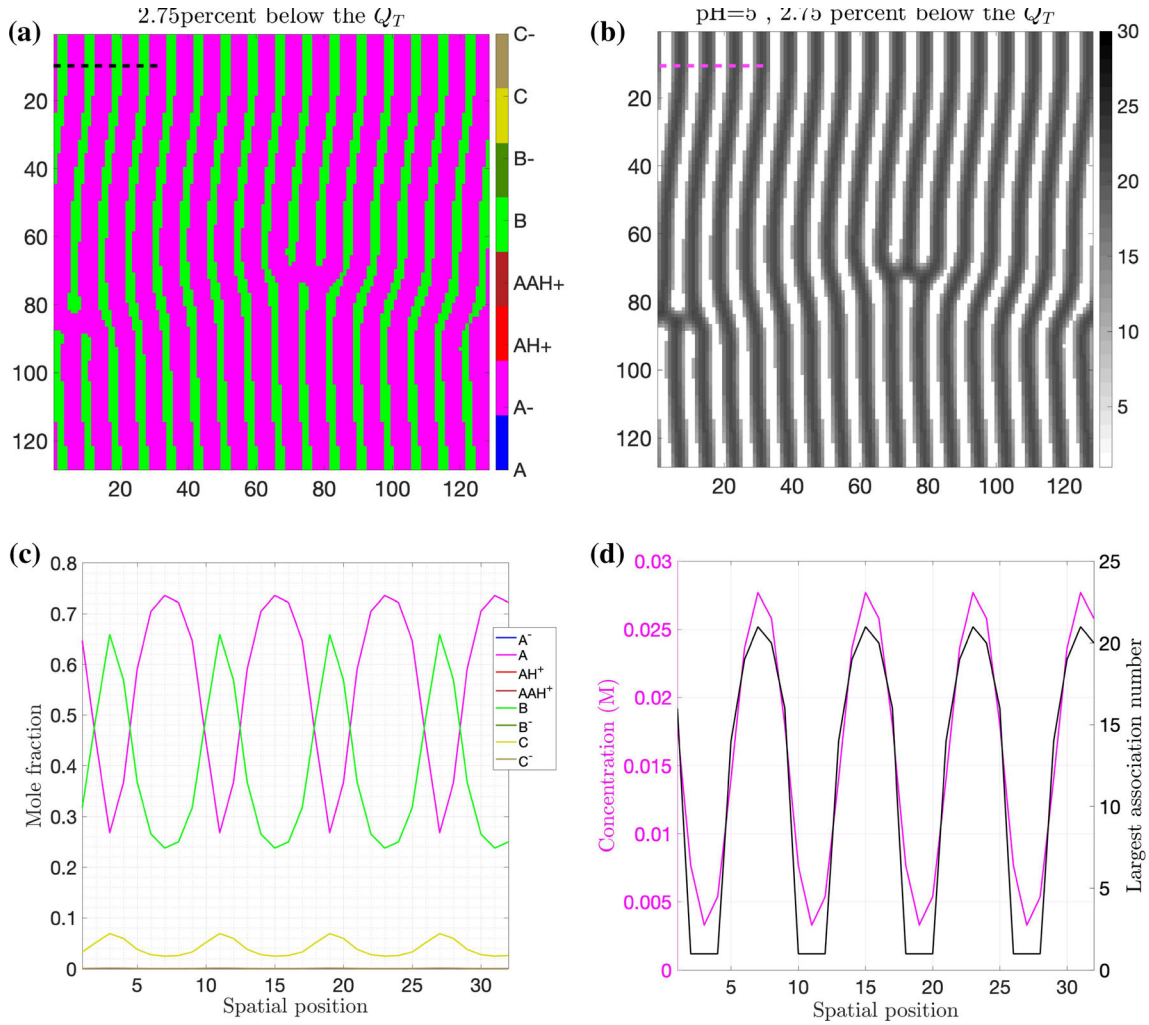

Figure 21. Two-dimensional patterns resulting from numerical simulations of the final model system to time $t = 2.5 \times 10^5$ with the parameter values described in the text and with the pH value equal to 5. Panel (**a**) indicates which species has the largest concentration at any position in space. We call that species as the *dominant species* at that position. Panel (**b**) shows, as a function of the spatial position, which n-mer of the dominant species at that position has the largest concentration. In panel (**c**) are plotted the mole fractions of the various species along the spatial cross section indicated by the dashed lines on panels (**a**) and (**b**). The A concentration and the value of n for which the n-mer of that species has the largest concentration are plotted along the same cross section in panel (**d**).

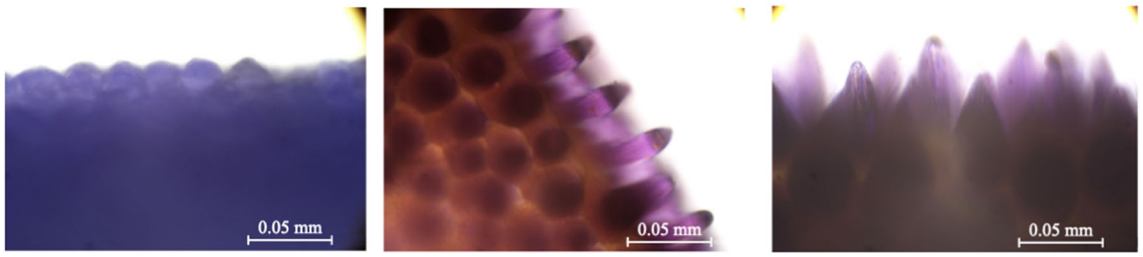

Figure 22. Microscopic images of plant epidermal cells in *Salvia yangii* (Russian sage; first panel) and *Viola wittrockiana* Gams (yellow pansy) (second and third panels). These images were prepared by S Thompson.

These results predict that anthocyanins may be present in the colorless hemiketal form (represented by green color in figure 20(a,b) and figure 21(a)) even where colored spots are not observed. This is consistent with our suggestion, made above regarding the experimentally observed patterns on Russian sage

flowers that appear in figure 4(d,e), that anthocyanin species are indeed present in colorless form in the white regions flanking the purple stripes.

6. Experimental methods

In this section, we describe the experimental methods for the observations presented in figures 3, 4, 12, 13, and 22. Three microscopes were used in various aspects of this work:

1. A Universal Microscope biological microscope fitted with an episcopic fluorescence cube system with UV 450 nm and 530 nm excitation wavelengths. The microscope was fitted with long-working-distance, plan ×4, ×10, ×20, ×40 lenses, and an Olympic LUC PLANFLN ×60 lens. The trinocular port was custom fit with Thor Lab adaptors and C mount, with a 200 μm fiber-optic cable connection to an Ocean Optics microspectrum meter. The microscope was also fitted with an eyepiece adaptor to fit a Canon RP mirrorless camera with ES lens adaptors and a custom 2× reduction lens. Stage temperature control was carried out with a custom-built device with a Peltier semiconductor with 6 mm hole, attached to a 0.25 in copper plate with two 2-port water coolers. Temperature could be maintained at ±0.2°C in a range of 0–70°C with a TE Technology TC-48-20 controller. Stage movement was measured by a custom-built electronic micrometer (±0.01 mm). All illuminators were LED systems.
2. An Olympus SZ × 12 stereomicroscope with 0.5× and 1.6× PF lenses. A custom Olympus DP 25 color-corrected camera was fit to the trinocular port. An Olympus S2X2AN polarizer with a multi-LED illuminator was used to obtain polarized light images.
3. A Universal Microscope metallurgical microscope with a custom-designed and built multiwavelength (white, 5000K, red, blue, green) light-controlled microcomputer. This scope was capable of both episcopic and diascopic polarized image acquisition at four wavelength bands. A temperature controller (similar to the one described earlier) was used.

A Universal Microscope MU 2003-BI digital camera with appropriate adapters for trinocuolar eyepiece fitting was used to aquire low-light (particularly fluorescence) images.

6.1 *Reagents*

All reagents were ACS reagents. Aqueous solutions (4 M HCl, 4 M NH_3, and various buffer systems) were prepared with analytical volumetric analysis equipment and HPLC-grade distilled water.

6.2 *Plant materials*

Flower samples were obtained from the Colorado State University (CSU) Perennial and Trial gardens, and Dr. S. Thompson's home garden. Samples were introduced to the microscope within one minute of collection for samples from the home garden, and five minutes for samples from the CSU gardens. Epidermal peels were obtained using a custom 2-sided tape system with teflon-coated stainless steel scalpels. Cultivar identification was provided by growers at the CSU gardens and by Dr. D. Steingraeber, plant physiologist and professor of biology at CSU.

The flexible optical system described in this section has allowed us to obtain and analyze both *in vivo* and *in vitro* absorption (ground-state), fluorescence (excited-state) and reflectance (surface-related) spectra of a variety of plant samples. This system enables the simultaneous acquisition of spectra and high-resolution still and video images. We have examined over 130 species of flower, 26 vegetable species, 32 species of leaf, and a number of seed and pollen species. The goals have been the following:

1. To spatially arrange vapor injection (of NH_3, HCl, CO_2, CO_x's, NO_x's, CH_3OH, CH_3CN) into epidermal peels (adaxial and abaxial) in order to probe pigment (anthocyanin, betacyanin, xanthin, carotenoid, etc.) identity and location. Figure 4 provides some example images from these experiments.
2. To compare the behavior of pigments in the just-described vapor injection experiments with the characteristics of solution extractions of the same plant materials. This allows for the correlation of *in vivo* data with the vast amount of *in vitro* data in the literature.
3. To examine the spatial concentration variation of anthocyanins on a cell-by-cell basis.
4. To develop evaporative and rehydration techniques on both *in vivo* and *in vitro* samples to examine the effect of induced concentration changes on anthocyanin species.
5. To evaluate interactions between anthocyanins and membranes, cell walls and cell-wall ridges, microtubules, etc.

These data, which complement and extend the experimental results and mathematical model analyzed in this study, will be the subject of future publications. In this upcoming work, we will compare experimental observations with the mathematical model to determine parameter values using methods of topological data analysis and machine learning (Adams *et al.* 2017; Wong Dolloff 2023).

7. Discussion

Patterns of anthocyanin pigmentation in plants arise from an interplay of processes, including the dynamics of activator and inhibitor molecules, activator concentration-dependent anthocyanin synthesis and transport, anthocyanin speciation kinetics, and anthocyanin association. In this paper, we first provided a linear stability analysis of a modified Gierer–Meinhardt (mGM) model for an activator–inhibitor system for anthocyanin synthesis proposed by Ding *et al.* (2020). This analysis allowed us to find an expression for the critical value Q_T of a parameter Q, proportional to the degradation rate constant for the inhibitor, at which a Turing bifurcation occurs. For values of Q less than Q_T, pattern formation occurs. Numerical simulations of the mGM model for values of Q close to and much less than Q_T show that a variety of patterns can occur. These include disordered stripe patterns, and both 'up' and 'down' disordered hexagon patterns.

We extended the mGM model to include (i) anthocyanin speciation, (ii) anthocyanin transport from the cytoplasm to the vacuole, and (iii) anthocyanin self association. The key to our story is that anthocyanins are synthesized in the cytoplasm, where the pH is approximately 7. The speciation kinetics therefore implies that anthocyanin molecules in the cytoplasm are primarily colorless species. Anthocyanins undergo a pH shift from 7 down to a pH range of 3–6 upon transport to the vacuole. In this pH range, a larger mole fraction will be in the colored (A^-, A, and AH^+) forms. However, even this pH shift does not sufficiently explain why colored species are observed in the vacuole, as the colorless hemiketal (B) remains the species with by far the largest mole fraction. We propose that self association can dramatically shift the balance so that there is a significant mole fraction of colored species. The mole fraction of colored species is highly concentration dependent, and at high (but biologically realistic) total anthocyanin concentrations, most of the anthocyanin can be in the colored form. Since pattern formation results in a spatially dependent total anthocyanin concentration, we showed that the mole fractions of colored vs. colorless species may also vary spatially.

The mGM model was proposed by Ding *et al.* (2020) in the context of their identification of activator and inhibitor proteins in *Mimulus* (monkeyflower). See figure 4 of Ding *et al.* (2020) for examples of *Mimulus* patterns and figure 6 of that paper for comparisons of *Mimulus* patterns with simulations of the mGM model. As our model starts with the mGM model, we as expected, obtain similar spot patterns, such as those shown in figure 20. However, our model differs from a simple activator–inhibitor model in that it provides additional information on spatial variations of molecular speciation and self association. Note that Ding *et al.* compare the *activator* pattern predicted by their model with the *anthocyanin color* pattern of observed *Mimulus* flowers. The model presented in this paper provides an important link from the activator concentration pattern to the actual anthocyanin color pattern, crucially using the spatially varying degree of self association. As indicated in the discussion of figure 21, our model thus predicts that the same activator concentration pattern can give rise to pigment patterns with varying spot sizes. In particular, we predict that spot sizes would change if, for example, NH_3 or HCl vapors diffuse across pigment patterns, changing cell pH values *in vivo* as illustrated by our experiments shown in figure 4. Additional observations and experiments to test the predictions of the model are outlined in section 6.

Besides spot patterns, we have shown that the extended mGM model can produce stripe patterns, such as those shown in figure 21. The predicted variation in the intensity of pigmentation across a stripe, as shown in that figure, compares well with the microscopic images of stripe patterns in *Salvia yangii* (Russian sage) shown in figure 4. Furthermore, as illustrated in figure 4(d), changing the pH of the cells by diffusing HCl across the petal increases the spatial range in which colored pigments are observed. This is analogous to the comparison between the larger spots in figure 20(a) for pH = 3.7 vs. the smaller spots in figure 20(b) for pH = 5. Although activator and inhibitor proteins associated with anthocyanin synthesis have not been identified in this species, the presence of an activator–inhibitor system in *Mimulus* suggests that similar mechanisms are at play in a broader range of plant species. Plant flower patterns are, however, highly diverse, as exemplified by the radiating stripes

of Brazilwood or the blotches in pansies shown in figure 1. The mGM model and our extension do not produce such patterns when simulated on square domains. Undoubtedly, other factors must be considered to understand the full array of plant patterns. The patterns develop in domains of various geometries that are changing in size and shape in tandem with the developing pattern. Venation patterns and the change of venation patterns over time likely affect pigment patterns, since anthocyanins are often more concentrated in veins. The mGM model assumes that activation of both the activator and the inhibitor are quadratic functions of the activator concentration; assuming higher-order powers would impact the type of pattern that forms. Plants could additionally employ coupled reaction–diffusion systems to tune the pigment pattern. A comprehensive understanding and model for plant pigment patterns has yet to emerge. However, we do expect that speciation and self association mechanisms play important roles as part of any mechanism for plant pigment pattern formation.

Although we have provided a significant extension of an existing model for anthocyanin pattern formation, our model remains a simplification of the many complex processes occurring in a plant. One such simplification involves the details of the complex, and still poorly understood, anthocyanin synthesis process, which involves the enzyme anthocyanin synthase (Wilmouth *et al.* 2002). We have simply subsumed this process into the synthesis of colorless precursor molecules P.

Another simplification involves the many facets of association. We have only included anthocyanin self association in our model and focused on the highly nonlinear dependence of this association on the total anthocyanin concentration. Anthocyanins also associates with other molecules (co-pigments) in plant cells, including rutins and quercetins (Sadlowski 1985).

We have also implicitly assumed that anthocyanins are in aqueous solutions, in that we have employed equilibrium constants measured *in vitro* in aqueous solutions. It is fascinating to consider the ramifications of the complex cellular environment in which all the processes we have discussed occur. Solubility factors, the hydrophobic/hydrophilic balance, and B-ring substitution all play roles in phase transitions that occur in the vacuolar environment (Hoshino *et al.* 1981a; Hoshino 1992). The actual composition of the intact vacuoles is also a factor. Analysis of tulip (Wagner 1979) and rose (Yamada *et al.* 2009) vacuoles show relatively large concentrations of glucose and fructose formed from the hydrolysis of starch, Na^+ and K^+ ions, and a large number of proteins. Many of these enzymes decorate the cytoplasmic-derived simple anthocyanins with hydroxl, methoxyl, glycosyl, and acyl groups. Indeed, the vacuole is not a simple aqueous solution, and this has consequences for anthocyanin function.

The ecological implications of anthocyanin pattern formation have been discussed by Ding *et al.* (2020). These authors impressively demonstrate that they can modify patterns in flowers and thereby affect their ability to attract bumblebees. Association affects anthocyanin spectra and may therefore also have an impact on how insects perceive a flower. Anthocyanins are present in the vacuoles of epidermal cells, which typically have a conical shape with ridges that may function as diffraction gratings (figure 22). The interplay of the geometry of plant epidermal cells and the kinetic and transport processes of plant pigments remain an area for further exploration.

Acknowledgements

We thank Ken Cline and David Steingraeber for valuable discussions and Ken Cline for designing and coding programs for spectral analysis and image manipulation and presentation. This work was supported by Grant DMS-1814941 awarded by the U.S. National Science Foundation.

Author contributions

Experiments were designed and performed by ST. All authors contributed towards designing the model and writing the manuscript. W-YH and PDS performed analysis and numerical simulations of the model.

References

Adams H, Emerson T, Kirby M, *et al*. 2017 Persistence Images: A stable vector representation of persistent homology. *J. Machine Learning Res.* **18** 1–35

Alappat B and Alappat J 2020 Anthocyanin pigments: Beyond aesthetics. *Rev. Mol.* **25** 5500

Bhati AP, Goyal S, Yadav R, *et al*. 2021 Pattern formation in *Passiflora incarnata*: An activator-inhibitor model. *J. Biosci.* **46** 84

Bradley RM and Shipman PD 2012 A surface layer of altered composition can play a key role in nanoscale

pattern formation induced by ion bombardment. *App. Surface Sci.* **258** 4161–4170

Chanoca A, Kovinich N, Burkel B, *et al*. 2015 Anthocyanin vacuolar inclusions form by a microautophagy mechanism. *Plant Cell* **27** 2545–2559

Craster RV and Sassi R 2006 Tech. Report No. 99, Universitá degli studi di Milano

Ding B, Patterson EL, Holalu SV, *et al*. 2020 Two MYB proteins in a self-organizing activator-inhibitor system produce spotted pigmentation patterns. *Curr. Biol.* **30** 802–814

da Silva PF, Paulo L, Barbafina A, *et al*. 2012 Photoprotection and the photophysics of acylated anthocyanins. *Chem. Eur. J.* **18** 3736–3744

Fernandes A, Brás NF, Mateus N, *et al*. 2015 A study of anthocyanin self-association by NMR spectroscopy. *New J. Chem.* **39** 2602–2611

Field T, Lee D and Holbrook N 2001 Why leaves turn red in autumn. The role of anthocyanins in senescing leaves of red-osier dogwood. *Plant Physiol.* **127** 566–574

Gavara R, Petrov V, Quintas A, *et al*. 2013 Circular dichroism of anthocyanidin 3-glucoside self aggregates. *Phytochemistry* **88** 92–98

Gérard M, Vanderplanck M, Wood T, *et al*. 2020 Global warming and plant-pollinator mismatches. *Emerg. Top. Life Sci.* **4** 77–86

Gierer A and Meinhardt H 1972 A theory of biological pattern formation. *Kybernetik* **12** 30–39

González-Manzano S, Santos-Buelga C, Dueñas M, *et al*. 2008 Colour implications of self-association processes of wine anthocyanins. *Eur. Food Res. Technol.* **226** 483–490

Hoshino T, Matsumoto U, Harada N, *et al*. 1981a Chiral exciton coupled stacking of anthocyanins: Interpretation of the origin of anomalous CD induced by anthocyanin association. *Tetrahedron Lett.* **22** 3621–3624

Hoshino T, Matsumoto U and Goto T 1981b Self-association of some anthocyanins in neutral aqueous solution. *Phytochemistry* **20** 1971–1976

Hoshino T 1991 An approximate estimate of self association constants and the self-stacking conformation of malvin quinoidal bases studied by 1H NMR. *Phytochemistry* **30** 2049–2055

Hoshino T 1992 Self-association of flavylium cations of anthocyanidin 3,5-diglucosides studied by circular dichroism and HNMR. *Phytochemistry* **31** 647–653

Hsu C-C, Chen Y-Y, Tsai W-C, *et al*. 2015 Three R2R3-MYB transcription factors regulate distinct floral pigmentation patterning in *Phalaenopsis* spp. *Plant Physiol.* **168** 175–191

Hsu W-Y 2022 Nonlinear dynamics of plant pigment patterns, Ph.D. Thesis supervised by P. D. Shipman, Colorado State University, Fort Collins

Kallam K, Appelhagen I, Luo J, *et al*. 2017 Aromatic decoration determines the formation of anthocyanic vacuolar inclusions. *Curr. Biol.* **27** 1–13

Koch AJ and Meinhardt H 1994 Biological pattern formation: from basic mechanisms to complex structures. *Rev. Mod. Phys.* **66** 1481–1507

Kondo S and Asai R 1995 A reaction-diffusion wave on the skin of the marine anglefish *Pomacanthus*. *Nature* **376** 765–768

Kondo S and Miura T 2010 Reaction-diffusion model as a framework for understanding biological pattern formation. *Science* **329** 1616–1620

Lev-Yadun S and Gould K 2009 Role of anthocyanins in plant defense; in *Anthocyanins: Biosynthesis, Functions, and Applications* (Eds) Gould K, Davies K and Winefield C (New York, NY, USA: Springer) pp. 22–28

Leydet Y, Gavara R, Petrov V, *et al*. 2012 The effect of self-aggregation on the determination of the kinetic and thermodynamic constants of the network of chemical reactions in 3-glucoside anthocyanins. *Phytochemistry* **83** 125–135

Lee D and Gould K 2002 Anthocyanins in leaves and other vegetative organs: An introduction. *Adv. Bot. Res.* **37** 1–16

Medel R, Botto-Mahan C and Kalin-Arroyo M 2003 Pollinator-mediated selection on the nectar guide phenotype in the Andean monkey flower, *Mimulus luteus*. *Ecology* **84** 1721–1732

Meinhardt H 2012 Turing's theory of morphogenesis of 1952 and the subsequent discovery of the crucial role of local self-enhancement and long-range inhibition. *Interface Focus* **2** 407–416

Meinhardt H and Gierer A 2000 Pattern formation by local self-activation and lateral inhibition. *Bioessays* **22** 753–760

Mendoza J, Oliveira J, Araújo P, *et al*. 2020 The peculiarity of malvidin 3-O-(6-O-p-coumaroyl) glucoside aggregation. intra and intermolecular interactions. *Dyes Pigments* **180** 108382

Miura T and Maini PK 2004 Periodic pattern formation in reaction-diffusion systems: An introduction for numerical simulation. *Anat. Sci. Int.* **79** 112–123

Moreira PF, Giestas L, Yihwa C, *et al*. 2003 Ground-and excited-state proton transfer in anthocyanins: From weak acids to superphotoacids. *J. Phys. Chem. A* **107** 4203–4210

Murray JD 2001 Mathematical biology. II spatial models and biomedical applications interdisciplinary applied mathematics V. 18. Springer

Padayachee A, Netzel G, Netzel M, *et al*. 2012 Binding of polyphenols to plant cell wall analogues-Part 1: Anthocyanins. *Food Chem.* **134** 155–161

Petrov V and Pina F 2010 Analytical resolution of the reaction rates of flavylium network by Laplace transform. *J. Math. Chem.* **47** 1005–1026

Pina F, Oliveria J and de Freitas V 2015 Anthocyanins and derivatives are more than flavylium cations. *Tetrahedron* **71** 3107–3114

Poustka F, Irani NG, Feller A, *et al*. 2007 A trafficking pathway for anthocyanins overlaps with the endoplasmic reticulum-to-vacuole protein-sorting route in *Arabidopsis* and contributes to the formation of vacuolar inclusions. *Plant Physiol.* **145** 1323–1335

Sadlowski ES 1985 Ph-dependent anthocyanin reactions in micellar and copigmented solutions, Ph.D. Thesis supervised by S. Thompson, Colorado State University, Fort Collins

Song Y, Yang R and Sun G 2017 Pattern dynamics in a Gierer–Meinhardt model with a saturating term. *Appl. Math. Model.* **46** 476–491

Sun Y, Li H and Huang JR 2012 *Arabidopsis* tt19 functions as a carrier to transport anthocyanin from the cytosol to tonoplasts. *Mol. Plant* **5** 387–400

Thompson S 2001 *Powerful pictures: A conceptually based curriculum for first-year chemistry* (Department of Education, FIPSE: US)

Thompson S 2010 *In vivo, in vitro, in vivo*, presentation, CSU Department of Chemistry

Turing AM 1990 The chemical basis of morphogenesis. *Bull. Math. Biol.* **52** 153–197

United Nations 2021 International Panel on Climate Change, AR6 Climate Change Synthesis Report: Climate Change

Veitia RA 2003 A sigmoidal transcriptional response: cooperativity, synergy and dosage effects. *Biol. Rev.* **78** 149–170

Wagner GJ 1979 Content and vacuole/extravacuole distribution of neutral sugars, free amino acids, and anthocyanins in protoplasts. *Plant Physiol.* **64** 88–93

Wilmouth RC, Turnbull JJ, Welford RWD, *et al*. 2002 Structure and mechanism of anthocyanidin synthase from *Arabidopsis thaliana*. *Structure* **10** 93–103

Wong Dolloff K 2023 Classification of plant pigment patterns using persistence images, Masters Thesis supervised by P. D. Shipman, Colorado State University, Fort Collins

Yamada K, Norikoshi R, Suzuki K, *et al*. 2009 Determination of subcellular concentrations of soluble carbohydrates in rose petals during opening by nonaqueous fractionation method combined with infiltration-centrifugation method. *Planta* **230** 1115–1127

Young DA 1984 A local activator-inhibitor model of vertebrate skin patterns. *Math. Biosci.* **72** 51–58

Yuan Y-W, Sagawa JM, Frost L, *et al*. 2014 Transcriptional control of floral anthocyanin pigmentation in monkeyflowers (*Mimulus*). *New Phytol.* **204** 1013–1027

Zheng X-T, Yu Z-C, Tang J-W, *et al*. 2021 The major photoprotective role of anthocyanins in leaves of *Arabidopsis thaliana* under long-term high light treatment: Antioxidant or light attenuator? *Photosynth. Res.* **149** 25–40

Corresponding editor: VIDYANAND NANJUNDIAH